

INTERACTIVE 3-D DIGITAL DISPLAY OF LINE-SHAPED PARTICLE
FROM INLINE HOLOGRAMS



A Thesis Submitted in Partial Fulfillment of the Requirements for the
Degree of Master of Engineering in Electrical Engineering
Suranaree University of Technology
Academic Year 2021

การแสดงผลดิจิทัล 3 มิติ เชิงโต้ตอบของอนุภาครูปรางเส้น
จากอินไลน์ไฮโลแกรม




นายแสงชัย ไพจิตร

วิทยานิพนธ์นี้เป็นส่วนหนึ่งของการศึกษาตามหลักสูตรปริญญาวิศวกรรมศาสตรมหาบัณฑิต
สาขาวิชาวิศวกรรมไฟฟ้า
มหาวิทยาลัยเทคโนโลยีสุรนารี
ปีการศึกษา 2564

INTERACTIVE 3-D DIGITAL DISPLAY OF LINE-SHAPED PARTICLE FROM INLINE HOLOGRAMS

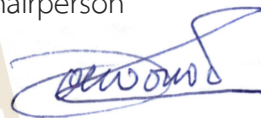
Suranaree University of Technology has approved this thesis submitted in partial fulfillment of the requirements for a Master's Degree.

Thesis Examining Committee



(Asst. Prof. Dr. Boonsong Sutapun)

Chairperson



(Prof. Dr. Joewono Widjaja)

Member (Thesis Advisor)



(Assoc. Prof. Dr. Arthit Srikaew)

Member



(Dr. Siriwat Soontaranon)

Member



(Assoc. Prof. Dr. Chatchai Jothityangkoon)

Vice Rector for Academic

Affairs and Quality Assurance



(Assoc. Prof. Dr. Pornsiri Jongkol)

Dean of Institute of Engineering

แสงชัย ไพจิตร : การแสดงผลดิจิทัล 3 มิติ เชิงโต้ตอบของอนุภาครูปร่างเส้นจากอินไลน์โฮโลแกรม (INTERACTIVE 3-D DIGITAL DISPLAY OF LINE-SHAPED PARTICLE FROM INLINE HOLOGRAMS) อาจารย์ที่ปรึกษา : ศาสตราจารย์ ดร.ยูวโน วิดจาया, 72 หน้า.

คำสำคัญ : จุลทรรศนศาสตร์โฮโลกราฟิกแบบดิจิทัล/ดิจิทัลโฮโลกราฟี/อนุภาครูปร่างเส้น 3 มิติ/การแสดงผลเชิงโต้ตอบ

ตามทฤษฎีด้านความรู้และความเข้าใจ การรับรู้ภาพทางสายตาและความเป็นจริงมีความสำคัญสำหรับการระบุและจดจำวัตถุ 3 มิติ เนื่องจากข้อมูลของวัตถุ 3 มิติถูกกำหนดโดยลักษณะทางเรขาคณิตของรูปร่างพื้นผิวของมัน วิทยานิพนธ์เล่มนี้ได้เสนอวิธีการปรับปรุงการวิเคราะห์ทางสัญญาณวิทยาของอนุภาครูปร่างเส้นโดยการแสดงภาพของอนุภาค 3 มิติ เชิงโต้ตอบที่สร้างขึ้นใหม่จากดิจิทัลอินไลน์โฮโลแกรม เพื่อที่จะดำเนินการตามวิธีการที่นำเสนอนี้ การสร้างใหม่เชิงตัวเลขถูกทำสำเร็จโดยที่ละแฉจากดิจิทัลโฮโลแกรมของอนุภาค หลังจากการวัดตำแหน่งของอนุภาคและเส้นผ่านศูนย์กลางในแต่ละแฉของภาพโฮโลแกรมแล้ว รูปร่างทั้งหมดของรูปภาพอนุภาคจะถูกสร้างขึ้นแบบดิจิทัลเป็นข้อมูลอาเรย์แบบ 3 มิติ จากนั้นแสดงผลไปยังมอนิเตอร์ของคอมพิวเตอร์ การสร้างภาพเชิงโต้ตอบถูกควบคุมโดยการเคลื่อนไหวของมือของผู้ใช้งานซึ่งตรวจจับโดยกล้องเว็บแคมราคาถูก ผลลัพธ์ที่ได้ คือ มุมการหมุนแบบ 360 องศา ของอนุภาคที่ถูกสร้างขึ้นใหม่สามารถถูกควบคุมเชิงโต้ตอบและแสดงผลไปยังหน้าจอได้ วิธีการที่นำเสนอนี้มีข้อได้เปรียบมากกว่างานที่ผ่านมาในประการแรก คือ ข้อมูลของอนุภาคที่สร้างขึ้นใหม่จากดิจิทัลโฮโลแกรมสามารถถูกมองเห็นได้ในพื้นที่ดิจิทัล แตกต่างจากวินโดว์มิกซ์เรียลลิตี้ที่ยังต้องใช้อุปกรณ์สวมใส่ที่ศีรษะ การนำเสนอภาพของอนุภาค 3 มิติ สามารถถูกควบคุมเชิงโต้ตอบผ่านทางกล้องเว็บแคมของคอมพิวเตอร์ได้ ประการที่สามคือ วิธีการที่นำเสนอไม่ได้ปรับปรุงเฉพาะการรับรู้ภาพทางสายตาและความรู้สึกสมจริงของผู้ใช้งานเท่านั้น แต่ยังรวมถึงความแม่นยำของการวิเคราะห์ทางสัญญาณวิทยาของอนุภาคอีกด้วย

สาขาวิชาวิศวกรรมอิเล็กทรอนิกส์
ปีการศึกษา 2564

ลายมือชื่อนักศึกษา Sangchai Paijit
ลายมือชื่ออาจารย์ที่ปรึกษา Dr. Yuwano

SANGCHAI PAIJIT : INTERACTIVE 3-D DIGITAL DISPLAY OF LINE-SHAPED PARTICLE FROM INLINE HOLOGRAMS. THESIS ADVISOR : PROF. JOEWONO WIDJAJA, Ph.D. 72 PP.

Keyword : DIGITAL HOLOGRAPHIC MICROSCOPY/DIGITAL HOLOGRAPHY/THREE-DIMENSIONAL LINE-SHAPED PARTICLE/INTERACTIVE DISPLAY

According to cognitive-field theory, visual perception and reality are important for 3-D object identification and recognition because 3-D object information is defined by the geometry of its surface profile. This thesis proposes a method to improve morphological analysis of line-shaped particles by visualizing interactively 3-D particle images reconstructed from digital inline holograms. In order to implement the proposed method, the numerical reconstruction is done row-by-row from the digital particle holograms. After measuring the particle position and its diameter from each row of the hologram image, the whole shape of the particle image is digitally created as 3-D array data and then displayed onto a computer monitor. The interactive visualization is controlled by the user's hand movements detected by a low-cost webcam. As a result, 360-degree rotation angles of the reconstructed particle can be interactively controlled and displayed onto the monitor. The proposed method has advantages over the previous works in that firstly, the particle information reconstructed from the digital holograms can be visualized in the digital space. Unlike Windows Mixed Reality which requires headsets, the proposed visualization of the 3-D particle can be interactively controlled via a webcam of a computer. Thirdly, the proposed method does not only improve visual perception and a reality sense of a user, but also the accuracy of morphological analysis of the particle.

School of Electronic Engineering
Academic Year 2021

Student's Signature Sangchai Paijit
Advisor's Signature Joewono Widjaja

ACKNOWLEDGEMENTS

I would like to express my deepest thanks to the people for their assistance and encouragement, which involved in the accomplishment of my thesis.

First of all, I would like to express my deepest gratitude to my thesis advisor Prof. Dr. Joewono Widjaja, for his ongoing support, encouragement, and advice throughout the study. Without his strong help and guidance, this thesis couldn't have been achieved.

Secondly, I am grateful to the member of my thesis defense committee, Asst. Prof. Dr. Boonsong Sutapun, Assoc. Prof. Dr. Arthit Srikaew and Dr. Siriwat Soontaranon for giving me various valuable suggestions.

I wish to express my special thanks to Suranaree University of Technology for its excellent facilities and thesis support scholarship.

I give special thanks to all lecturers in the School of Electrical Engineering and School of Electronic Engineering who have taught and given me excellent knowledge in the past four academic years. I am also grateful to my research group members, especially Saowaros Dawprateep, who gave valuable suggestions. I also would like to thank Jordan Hakim Hossea, Taweesak Chaiyakhan, and Preeyakamol Kaewbandit, who gave an excellent idea for my thesis.

Finally, I sincerely special thanks to my beloved parents, Mr. Sanguthai Pajit and Mrs. Somruthai Pajit, for their hard support, understanding, great encouragement, and financial support for all the years of my education.

SANGCHAI PAIJIT

TABLE OF CONTENTS

	Page
ABSTRACT (THAI)	I
ABSTRACT (ENGLISH)	II
ACKNOWLEDGEMENTS	III
TABLE OF CONTENTS	IV
LIST OF TABLES	VI
LIST OF FIGURES	VII
CHAPTER	
I INTRODUCTION	1
1.1 Background	1
1.2 Significance of the study	3
1.3 Research objectives	4
1.4 Scope and limitation of the study	4
1.5 Organization of the thesis	4
II THEORY	6
2.1 Digital inline holography	6
2.2 Conventional numerical reconstruction	8
2.3 Measurement of Image Sharpness	10
2.4 Hand detection.....	11
2.4.1 Color thresholding using HSV color space.....	13
2.4.2 Morphological operation.....	14
2.4.3 Blob extraction	20
III RESEARCH METHODOLOGY	24
3.1 Proposed 3-D digital imaging system	24

TABLE OF CONTENTS (Continued)

	Page
3.2 Numerical reconstructions of particle holograms.....	27
3.3 Formation of 3-D line-shaped particle	31
3.4 Interactive imaging system	33
3.5 Rotation angles of 3-D particle imaging	35
3.6 Instrumentations	37
IV EXPERIMENTAL VERIFICATIONS	38
4.1 Experimental information extraction from the particle holograms	38
4.2 Particle depth measurement.....	41
4.3 Particle orientation measurement.....	44
4.4 Particle size measurement.....	45
4.5 3-D Display of the particle image	47
4.5.1 Particle image with non-uniform surface	47
4.5.2 Changes of Particle Image Orientation	49
4.6 Calibrations of the webcam-based imaging setup	51
4.7 Experimental verifications of the hand detections.....	55
4.8 Experimental measurements of the hand position.....	56
4.9 Experimental verifications of the Interactive imaging of 3-D microtube.....	61
V CONCLUSIONS AND FUTURE WORK	64
5.1 Conclusions	64
5.2 Future work.....	65
REFERENCES	66
APPENDIX	69
CURRICULUM VITAE	72

LIST OF TABLES

Table		Page
4.1	Mean absolute percentage errors in the depth measurements of the line-shaped particle.....	44
4.2	Mean absolute percentage errors in the orientation angle measurements of the line-shaped particle	44
4.3	Mean absolute percentage errors in the diameter measurements of the line-shaped particle.....	46
4.4	Time measurement of the hand detections.....	56
4.5	Errors in the measurement of the shortest movement distance by using the digital height gauge.....	58
4.6	Errors in the measurements of the hand position $+d_x$ and its corresponding angle $+\theta_x$ by using the optical rail.....	59
4.7	Errors in the measurements of the hand position $+d_y$ and its corresponding angle $+\theta_y$ by using the digital height gauge	60
A.1	Errors in the measurements of the hand position $-d_x$ and its corresponding angle $-\theta_x$ by using the optical rail.....	70
A.2	Errors in the measurements of the hand position $-d_y$ and its corresponding angle $-\theta_y$ by using the digital height gauge	71

LIST OF FIGURES

Figure		Page
2.1	Schematic diagram of digital recording of inline holograms	6
2.2	The 1-D normalized intensity transmittance of the line-shaped particle hologram simulated by using Eq. (2.1)	7
2.3	The simulated hologram of the line-shaped particle.....	8
2.4	Geometry of the numerical reconstruction of the digital inline hologram	9
2.5	Numerical reconstruction of 1-D images from the simulated hologram of the line-shaped particle at different reconstruction distances z	10
2.6	Flowchart of the hand detection based on blob analysis	12
2.7	The boundary of HSV color space (Stratmann, 2022)	13
2.8	Conversion of RGB to HSV color with the output of color thresholding	14
2.9	(a) A disk-shaped structuring element with a radius of 3 and (b) rectangle-shaped structuring element with a size of 1×3 (The MathWorks, Inc., 2022)	15
2.10	Block diagram of the dilation operation which increases the number of the white pixels of the binarized image.....	16
2.11	Block diagram of the erosion operation for reducing noise in the binarized image	18
2.12	Morphological process of a color image. (a) The image of a hand model from a single video frame, (b) the resultant binarized image by thresholding the HSV color space. The dilated images using the disk-shaped structuring elements with a radius of (c) 3 and (d) 7.....	20
2.13	Result of applying the 4-connectivity in the binarized image (Moeslund, 2012).....	21
2.14	The Grass-fire algorithm for extracting the blobs in the binarized image (Moeslund, 2012).....	22

LIST OF FIGURES (Continued)

Figure	Page
3.1	Flowchart for the interactive 3-D digital imaging system..... 24
3.2	The orientation angle of the particle used in the hologram formation..... 25
3.3	Flowchart for the numerical reconstruction of the particle holograms..... 27
3.4	The LAP calculation from the Fresnel-based numerical reconstructions of the line-shaped particle hologram simulated at the recording distance $z = 40$ cm 28
3.5	Normalized numerical reconstruction image of the line-shaped particle hologram 29
3.6	Geometry relationship between the particle depth, orientation angle and the array image sensor 29
3.7	Flowchart for displaying the 3-D line-shaped particle from the numerical reconstruction results 31
3.8	Construction of the particle side surface by connecting all points on the 2-D circle between rows..... 32
3.9	Flowchart for the interactive 3-D particle imaging 33
3.10	Schematic diagram of translational hand movements 34
3.11	Rotation direction of the reconstructed 3-D particle by using the rotate function in Matlab 36
4.1	Experimental setup for recording the line-shaped particle holograms..... 38
4.2	The experimentally recorded digital inline hologram of the $100\ \mu\text{m}$ line-shaped particle at the recording distance z of 40 cm with the angle θ of 60° 39
4.3	1-D intensity transmittance of the experimental hologram shown in Figure 4.2 scanned along the horizontal axis at $y = 20^{\text{th}}$ row..... 40
4.4	1-D intensity transmittance of the experimental hologram shown in Figure 4.2 scanned along the horizontal axis at $y = 480^{\text{th}}$ row..... 41

LIST OF FIGURES (Continued)

Figure		Page
4.5	The depth measurements of the 100 μm microtube at the recording distance $z = 40$ cm with the angles $\theta = 60^\circ$ and 75°	42
4.6	The depth measurements of the 100 μm microtube at the recording distance $z = 34$ cm with the angles $\theta = 60^\circ$ and 75°	43
4.7	The particle diameter measurements of the 100 μm microtube at the recording distance $z = 40$ cm with the angles θ of 60° and 75°	45
4.8	The particle diameter measurements of the 100 μm microtube at the recording distance $z = 34$ cm with the angles θ of 60° and 75°	46
4.9	3-D display of the microtube shape at the recording distance $z = 40$ cm with the orientation angles θ (a) 60° and (b) 75°	47
4.10	3-D display of the microtube shape at the recording distance $z = 34$ cm with the orientation angles θ (a) 60° and (b) 75°	48
4.11	Relationship between the particle orientations and the calculated rotation angle $+\theta_x$	49
4.12	Relationship between the particle orientations and the calculated rotation angle $+\theta_y$	50
4.13	Schematic diagram of a calibration process for finding the object plane s_o in the webcam-based imaging setup.....	51
4.14	The LAP calculation from the grating pattern images at the different positions s_o as a function of the webcam focus.....	52
4.15	Schematic diagram of a calibration process for finding the sensor plane s_i in the webcam-based imaging setup.....	53
4.16	Schematic diagram of the FOV and AOV of the webcam	54

LIST OF FIGURES (Continued)

Figure		Page
4.17	Morphological operation of the hand color image. (a) The image of the hand model from a single video frame. (b) The resultant binarized image by thresholding the HSV color space, (c) The dilated images using the disk-shaped structuring elements with a radius of 5. (d) The resultant hand detection confined by the bounding box with the hole noise removal.....	55
4.18	Direction of the translational hand movement along (a) the x - and (b) the y -axes detected by using the webcam.....	57
4.19	The detected hand model confined by the bounding box. The red and the black plus symbols denote the center of the sensor plane and the bounding box, respectively	57
4.20	Interactive imaging of the 3-D microtube reconstructed from the digital hologram by using the hand movement along the x -axis.....	61
4.21	Interactive imaging of the 3-D microtube reconstructed from the digital hologram by using the hand movement along the y -axis	63

CHAPTER I

INTRODUCTION

1.1 Background

Inline holography is an optical technique for recording the amplitude and phase of a light wave by forming an interference of a *reference wave* and a *diffracted wave* of an object on light-sensitive media (Hariharan, 1996). The inline holography was invented by Gabor in 1948 (Gabor, 1948). The diffracted wave is generated when the light wave passes around the object's edges, causing slight bending of the light. The interferences of the two light waves can be achieved under the conditions that a light source produces coherent (*constant phase*) and monochromatic light (*single wavelength*). The recorded intensity of the interference pattern is known as a hologram, which contains three-dimensional (3-D) information about the object, such as size and its position in 3-D space. In order to optically reconstruct an image from the hologram, the hologram is illuminated by the same light source.

In digital inline holography (DIH), holograms of an object are digitally recorded by using an array image sensor. The object image can be numerically reconstructed from the holograms by using the Fresnel diffraction integral with fast Fourier transform (FFT) algorithm (Zhang, Lü, and Ge, 2004). DIH has been developed and widely used in the field of science and technology, such as studies of small particles and microorganisms. The 3-D shape display of small objects using numerical reconstruction from digital holograms can be used not only diagnosis of cell disease but also for microscopy because they cannot be seen with the naked eye.

In medical science, morphological analysis has long been used for the abnormality diagnosis of cells. For example, one of the factors causing male infertility is due to abnormal sperm morphology. DIH has been proposed as a non-invasive and simple method for assessing spermatozoon abnormality by reconstructing its 3-D

profile (Merola *et al.*, 2013). Dimension of the reconstructed 3-D profile is used to calculate surface area and its corresponding biovolume. In order to estimate the surface area and biovolume, a set of recorded holograms of the spermatozoon were sequentially recorded for different angular positions. The angular positions were set by rotating a spermatozoon via an optical tweezer. Quantitative phase map of the spermatozoon profile was calculated for different angles and converted to silhouette, yielding the estimated area and biovolume.

3-D morphometry of red blood cells has been studied by using DIH (Memmolò *et al.*, 2014). This holographic method is capable of reconstructing the concave surface of red blood cells. Some pathological conditions such as cancer and infection can be diagnosed from the thickness and biovolume of a red blood cell. Therefore, it is useful for the diagnosis of red blood cell abnormality.

Studying of cell motility using digital holography microscopy (DHM) was reported by Yu and his coworkers (Yu *et al.*, 2014). In this study, 3-D tracking and visualization of free-swimming cells such as *Chlamydomonas* and *Paramecium* were reported. Holographic videos of the motile cells were recorded by using a CCD image sensor at 30 fps. Numerical reconstruction based on the angular spectrum method (Kim, 2010) was used to locate the cell position on each hologram frame. Besides cell size and its profile, this non-invasive method provides information of motility speed.

DIH has also been employed for the recognition of line-shaped microorganisms (Javidi *et al.*, 2005). Recognition of unknown microorganisms such as *Sphaerularia* alga and *Tribonema aequale* alga can be done by localizing a specific shape of the microorganisms from digital holograms. Thus, the method can be applied to environmental monitoring.

Furthermore, DHM has been used to study air pollution and fuel injection by reconstructing images of fast-moving bubbles in air-water mixture flows (Tian *et al.*, 2010). In contrast to phase-Doppler imaging (Naqwi *et al.*, 1991), which requires a complicated optical setup, digital holograms of bubbles were recorded by using a CCD sensor of the simple DHM setup. The size and the 3-D position of bubbles can be numerically extracted by using the Fresnel diffraction integral.

1.2 Significance of the study

The previous section describes the importance of DIH for the non-invasive study of 3-D motility and morphology of living and non-living microorganisms. Although the previous methods have been verified and demonstrated, the extraction of the desired 3-D information by using numerical reconstructions from a set of digital holograms provides only the estimation instead of the exact information.

In cognitive-field theory, it is a known fact that visual perception and reality are important for 3-D object identification and recognition because 3-D object information is defined by the geometry of its surface profile (Rock, Halper, and Clayton, 1972). Therefore, 3-D morphological information analysis can be improved by having a reality sense of 3-D imaging of the reconstructed images from holograms.

Recently, mixed reality (MR) has become one of the popular digital technologies. Unlike virtual reality (VR), which fully immerses users in a computer-simulated environment, MR is an immersive technology where users can interact and manipulate virtual objects by using gesture, gaze, or speech input (Intel Corporation, 2020; Microsoft Corporation, 2022). Therefore, it enhances the user's natural vision and perception. In medicine, MR has been reported to be useful for improving anatomical teaching and surgical planning (Yamazaki *et al.*, 2021). In the report, bone models were digitally generated and visualized through a see-through glass of a MR display, which merges digital bone images and the real environment. This facilitates interaction between medical personnel and the virtual objects.

Therefore, in order to improve the accuracy of morphological analysis of small particles, this research proposes a new digital method for displaying interactively 3-D surface morphology of the particles reconstructed from digital inline holograms by using the MR concept. In order to implement the proposed method, the numerical reconstruction is done row-by-row from the digital particle holograms. After measuring the particle position and its diameter from each row, the whole shape of the particle image is digitally created as 3-D array data and then displayed onto a computer monitor. As a result, 360-degree rotation angles of the reconstructed particle can be interactively controlled and displayed onto a monitor. The proposed method has advantages over the previous works in that firstly, the particle information

reconstructed from the digital holograms can be visualized in the digital space. The proposed visualization of the 3-D particle can be interactively controlled via a webcam of a computer. Thirdly, the proposed method does not only improve visual perception and a reality sense of a user, but also the accuracy of morphological analysis of the particle.

1.3 Research objectives

- To digitally display the 3-D particle onto a computer monitor with controlled rotation angles.
- To interactively visualize the reconstructed 3-D particle image by detecting hand movements via a webcam of a computer.

1.4 Scope and limitation of the study

- The line-shaped particle is a polycarbonate microtube (Paradigm Optics, CTPC-067-100) with a diameter of 100 μm .
- The feasibility of the proposed method is experimentally verified by using the digital holograms of rotated particles.
- The 3-D particle image is numerically reconstructed and displayed onto a computer monitor.
- Interactive 3-D visualization of the particle image is done by detecting hand movements via a webcam.

1.5 Organization of the thesis

The remainder of the thesis is organized as follows. Chapter II reviews the fundamental of digital inline holography. The conventional numerical reconstruction from digital holograms using the Fresnel diffraction integral and search for the best focus from the reconstructed images are reviewed. In Chapter III, the proposed method for visualizing interactively the reconstructed 3-D particle is discussed. Chapter IV discusses the experimental measurements of the position, size, and orientation of the reconstructed particle image. The detection of the hand movement using the webcam

and the interactive 3-D visualization of the line-shaped particle are then experimentally validated.



CHAPTER II

THEORY

Currently, digital holography has been developed and widely used in the fields of science and technology. In this chapter, the theory of digital inline holography is reviewed. The digital inline holograms of a line-shaped particle and numerical reconstruction by using the Fresnel diffraction integral are mathematically described. Finally, the measurement of the image sharpness of the reconstruction images to find the best focus is discussed in this chapter.

2.1 Digital inline holography

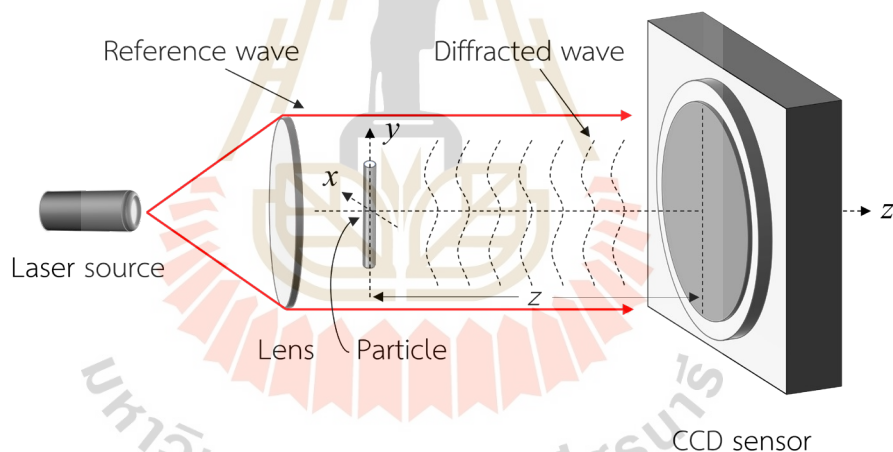


Figure 2.1 Schematic diagram of digital recording of inline holograms.

Figure 2.1 shows a schematic diagram of an optical setup for recording digital inline holograms by using a CCD sensor. The line-shaped particle with a diameter of $2a$ is placed in front of the CCD sensor and illuminated by a monochromatic light generated from a laser source with a wavelength of λ . The recording distance z is the distance between the line-shaped particle and the CCD sensor along the optical axis. By recording the interference pattern of the wave diffracted by the particle and the direct reference wave from the laser source, the intensity transmittance of the line-

shaped particle hologram can be mathematically expressed as (Tyler and Thompson, 1976)

$$I(x) = \left\{ 1 - \frac{4a}{\sqrt{\lambda z}} \cos\left(\frac{\pi x^2}{\lambda z} - \frac{\pi}{4}\right) \left[\frac{\sin\frac{2\pi ax}{\lambda z}}{\frac{2\pi ax}{\lambda z}} \right] + \frac{4a^2}{\lambda z} \left[\frac{\sin\frac{2\pi ax}{\lambda z}}{\frac{2\pi ax}{\lambda z}} \right]^2 \right\} \text{rect}\left(\frac{x}{2L}\right). \quad (2.1)$$

In Eq. (2.1), the first term is a uniform background of the reference wave, which is directly generated from the laser source. The second term is the cosine chirp modulated by a sinc function, which this term represents the diffraction pattern of the line-shaped particle. The third term is a square of the sinc function that represents the intensity of the diffraction pattern of the line-shaped particle. Here, $2L$ corresponds to the width of the CCD sensor. Furthermore, the spatial frequency of the cosine chirp is proportional to $x/\lambda z$.

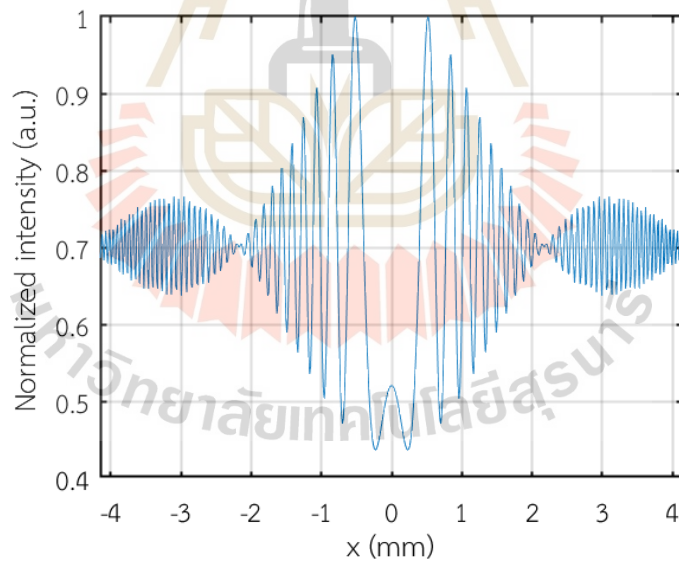


Figure 2.2 The 1-D normalized intensity transmittance of the line-shaped particle hologram simulated by using Eq. (2.1).

Figure 2.2 shows the 1-D normalized intensity transmittance of the simulated hologram of the line-shaped particle with a $100 \mu\text{m}$ diameter, which is plotted by using Eq. (2.1). The recording distance z and the laser source with a wavelength λ were 40

cm and 543.5 nm, respectively. The hologram width $2L$ was 8.3 mm. The hologram intensity is modulated by the sinc function, and its spatial frequency variation is determined by the cosine chirp.

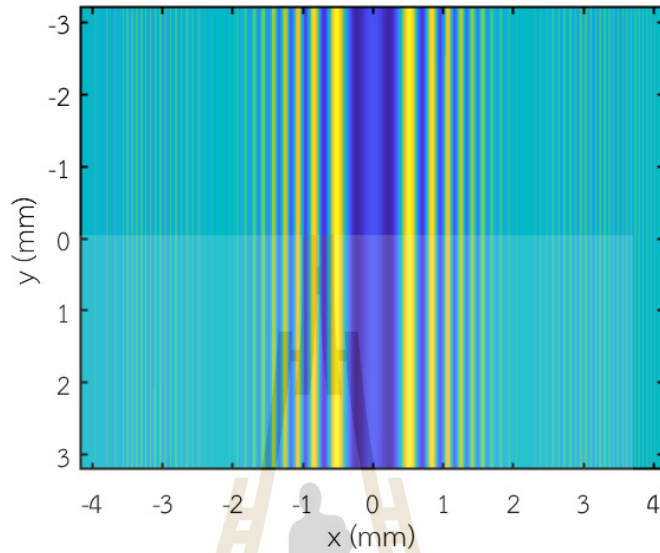


Figure 2.3 The simulated hologram of the line-shaped particle.

Figure 2.3 shows the simulated 2-D hologram of the line-shaped particle corresponding to Figure 2.1. The bright and the dark stripes correspond to the maximum and the minimum intensity of the cosine chirp shown in Figure 2.2. Due to the sinc modulation, only the stripes that appeared in the middle of the hologram can be clearly observed.

2.2 Conventional numerical reconstruction

Since the hologram encodes the diffracted wave of the object, the image reconstruction can be done by using the Fresnel diffraction integral. In diffraction theory, the Fresnel diffraction integral given by (Goodman, 1996)

$$U(x, y) = \frac{\exp(jkz)}{j\lambda z} \int_{-\infty}^{\infty} \int_{-\infty}^{\infty} U(\xi, \eta) \times \exp\left\{j \frac{k}{2z} \left[(x - \xi)^2 + (y - \eta)^2 \right]\right\} d\xi d\eta . \quad (2.2)$$

is generally used to calculate the diffraction pattern that occurs when the light wave

encounters an aperture or around an opaque object. Here, $U(x, y)$ and $U(\xi, \eta)$ correspond to the reconstructed optical field across the reconstruction image at (x, y) plane and the hologram located at (ξ, η) plane shown in Figure 2.4, respectively. The distance z is the reconstruction distance. In Eq. (2.2), it can be rewritten as a convolution integral

$$U(x, y) = \iint_{-\infty}^{\infty} U(\xi, \eta) \times h(x - \xi, y - \eta) d\xi d\eta, \quad (2.3)$$

with

$$h(x, y) = \frac{\exp(jkz)}{j\lambda z} \exp\left[\frac{jk}{2z}(x^2 + y^2)\right], \quad (2.4)$$

where $h(x, y)$ represents the impulse response function of free space propagation, and the wave number k is $2\pi/\lambda$. This interpretation facilitates the implementation of the numerical reconstruction by using fast Fourier transform (Lee *et al.*, 2011)

$$U(x, y) = \mathfrak{F}^{-1}\{\mathfrak{F}\{U(\xi, \eta)\} \mathfrak{F}\{h(x, y)\}\}, \quad (2.5)$$

where $\mathfrak{F}\{\}$ and $\mathfrak{F}^{-1}\{\}$ denote the Fourier and its inverse transforms, respectively.

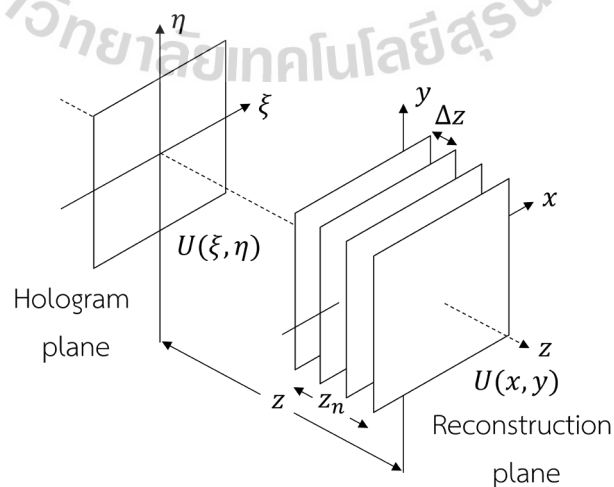


Figure 2.4 Geometry of the numerical reconstruction of the digital inline hologram.

Since the particle depth positions are generally unknown, a set of the numerically reconstructed images is generated at different distances z_n with an increment of Δz . In order to find the particle depth position, the best focus image is determined by measuring the sharpness of the reconstructed image intensity via the Laplacian operator (LAP).

2.3 Measurement of Image Sharpness

The numerical reconstruction is very useful for reconstructing particle images, but the correct particle depth position cannot be directly known. The best focus intensity of the numerically reconstructed image gives the correct particle depth position. In image processing, the best focus intensity of the digital image $I(x, y)$ can be measured by measuring its sharpness using the Laplacian operator (LAP) defined as (Choi and Lee, 2009)

$$LAP(y) = \sum_{x=1} \sum_{y=1} [I(x+1, y) + I(x-1, y) - 2I(x, y)]^2. \quad (2.6)$$

Since the best focus of the reconstructed image has the sharpest contrast, LAP of Eq. (2.6) gives the maximum intensity value.

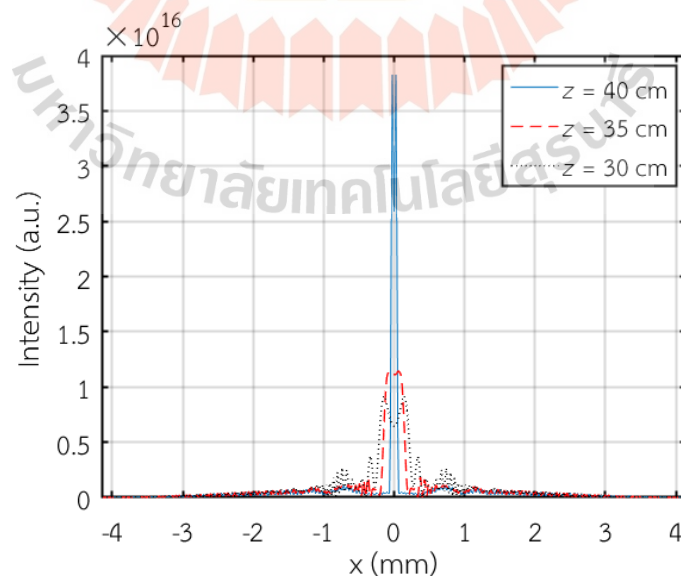


Figure 2.5 Numerical reconstruction of 1-D images from the simulated hologram of the line-shaped particle at different reconstruction distances z .

Figure 2.5 shows a comparison of the 1-D numerical reconstruction of the simulated hologram of the 100 μm line-shaped particle shown in Figure 2.2 at the reconstruction distances $z = 30, 35,$ and 40 cm. In Figure 2.5, the reconstruction at the correct reconstruction distance $z = 40$ cm has the highest intensity value and narrowest width compared to the other reconstruction results.

2.4 Hand detection

In the proposed method, the object detection system is developed to detect hand movements. This facilitates interactive controls of the rotation angles of the 3-D particle imaging via the webcam. Thus, it does improve not only the accuracy of morphological analysis of the particle, but also visual perception and a reality sense of a user.

Recently, several methods for object detection using convolutional neural network (CNN) (Yamashita *et al.*, 2018), Viola–Jones’s algorithm (Viola and Jones, 2001), and blob analysis (Moeslund, 2012) have been reported. CNN and Viola–Jones’s algorithms are based on machine learning. Therefore, they are somewhat complicated and computationally expensive (Li *et al.*, 2017; Zhang *et al.*, 2021). In contrast, the blob analysis is implemented using simple image processing operations.

In digital image processing, a region of an object image in a binarized image is called a blob. As a result, all picture elements in the blob can be considered similar to each other. In order to detect objects, blob-based method compares brightness or color information to surrounding regions.

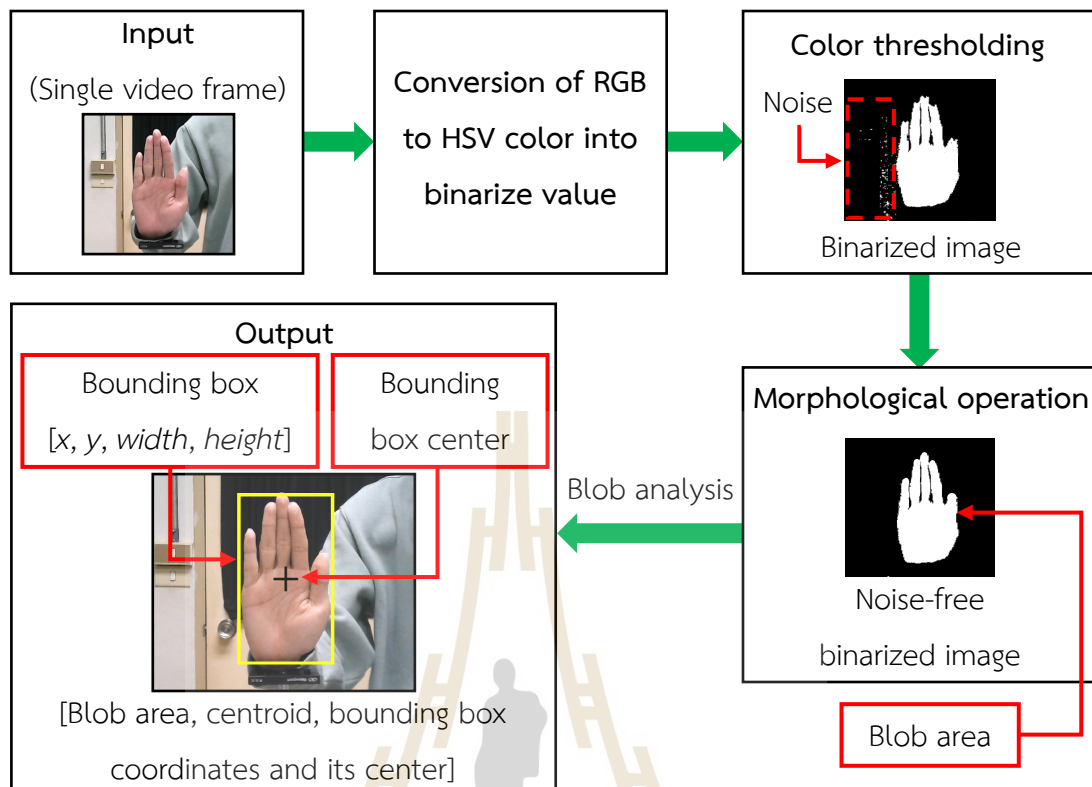


Figure 2.6 Flowchart of the hand detection based on blob analysis.

Figure 2.6 shows the flowchart of the hand detection from a color single video frame based on the blob analysis. There are four steps that are based on Matlab (MathWorks 2019b). In the first step, a single frame of an input video is extracted using the snapshot function in Matlab and saved the single frame of the input video into storage. The second step converts the extracted video frame from RGB to HSV color model into a binarized image by using color thresholding in Matlab, producing white and black pixels with intensity values of 1 and 0, respectively. In the third step, the *Color Thresholder app* in Matlab is employed to segment color images by manipulating the color components of these images based on different color spaces. Due to unbalanced illumination or poor image quality, the resultant binarized image shown in Figure 2.6 is frequently degraded by noise. In order to suppress the noise, the fourth step employs a region morphology to transform the region of interest by applying a kernel to each pixel in the binarized image. After the noise suppression, the region of interest consists of the resultant white pixels. In the fourth step, the blob analysis

calculates statistics for the region of interest, yielding blob features that are blob area, centroid, bounding box coordinates $[x, y, width, height]$, where x and y points are the location at the upper-left corner of the bounding box, and its center. In Matlab, the blob analysis can be performed by using the function *vision.BlobAnalysis*.

2.4.1 Color thresholding using HSV color space

The HSV color space (Moeslund, 2012) is a color model representing *hue*, *saturation*, and *value* as shown in Figure 2.7. The primary color (RGB) corresponds to hue, regardless of lightness and darkness. The saturation is an amount of hue that corresponds to the half-circle at the center of the color space shown in Figure 2.7. The lower saturation corresponds to an increase in whiteness. Finally, the value represents the lightness and darkness of the hue. In addition, the use of the HSV color model to do the color thresholding is because the RGB color model cannot separate the primary color from the lightness and darkness. Therefore, it is quite difficult to do the color thresholding for hand detection. Also, the primary color in the HSV color model can be directly adjusted in the hue. This is different from the RGB color model, where the primary color is separated by three color spaces.

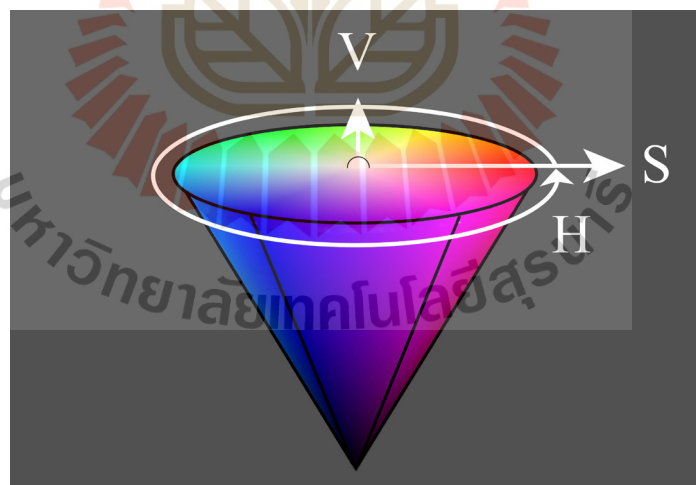


Figure 2.7 The boundary of HSV color space (Stratmann, 2022).




















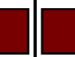








































RGB	HSV	Output with color thresholding value								
		H			S			V		
		0.000	0.500	1.000	0.000	0.500	1.000	0.000	0.500	1.000
	H = 0.0000 S = 1.0000 V = 1.0000									
	H = 1.0000 S = 1.0000 V = 0.4665									
	H = 0.3340 S = 1.0000 V = 1.0000									
	H = 0.3685 S = 1.0000 V = 0.4665									
	H = 0.6665 S = 1.0000 V = 1.0000									
	H = 0.6510 S = 1.0000 V = 0.4665									

Figure 2.8 Conversion of RGB to HSV color with the output of color thresholding.

Figure 2.8 illustrates the conversion of RGB to HSV color and the output of the color thresholding in RGB image color. The first column depicts the RGB color variations of the input image, which consist of red, dark red, green, dark green, blue, and dark blue, respectively. The HSV values of the input image are verified via Matlab. The completely red color in RGB color is 255, but the hue is 0.000 in the binarized image. The saturation and the value of the complete color in the binarized image represent the value of 1.000. When the color thresholding of the hue is set to 0.000, the appearance of the output image is the red color, which is the color of the white pixels in the case of the binarized image. When the hue is set to be the other values, the output image will become the same as the input image. In the case of the green color, when the hue is set to be 0.000, the output appears in the black color, which indicates that the algorithm cannot access the value of the green color.

2.4.2 Morphological operation

In digital image processing, the morphological operation is used to identify an object shape in the form of a binarized input image which involves a noise suppression caused by a background signal. This is done by applying a kernel to each

pixel in the binarized image. When the noise is reduced, pixels in the region of interest become white pixels. A kernel to suppress the noise is called a structuring element. Matlab provides several kinds of structuring elements, such as a disk and a rectangle shown in Figures 2.9 (a) – (b), which are represented by using the grey color area.

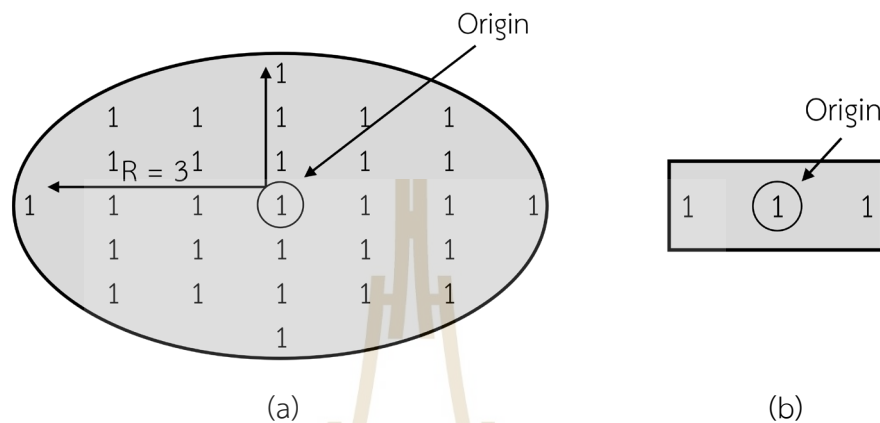


Figure 2.9 (a) A disk-shaped structuring element with a radius of 3 and (b) rectangle-shaped structuring element with a size of 1×3 (The MathWorks, Inc., 2022).

The structuring element is a binary-valued neighborhood, which consists of the true pixels (1's value) and the false pixels (0's value). The true pixels will be included in the morphological computation, whereas the false pixels will be discarded. The circle symbol at the center pixel in the binarized figures is called the origin. In Matlab, the size of the structuring element can be adjusted. The types of the structuring element and its size are very important to reduce noise in the binarized input image. Since the hand has a rounded shape, this research work uses the disk-shaped structuring element to reduce the noise from the background and improve the reconstructed hand shape by increasing the number of white pixels, which is known as the dilation operation. On the other hand, the noise suppression in the binarized image is called the erosion operation. Figures 2.10 and 2.11 show the morphological operation in the binarized image by using the 1×3 rectangle-shaped structuring element by dilation and erosion.

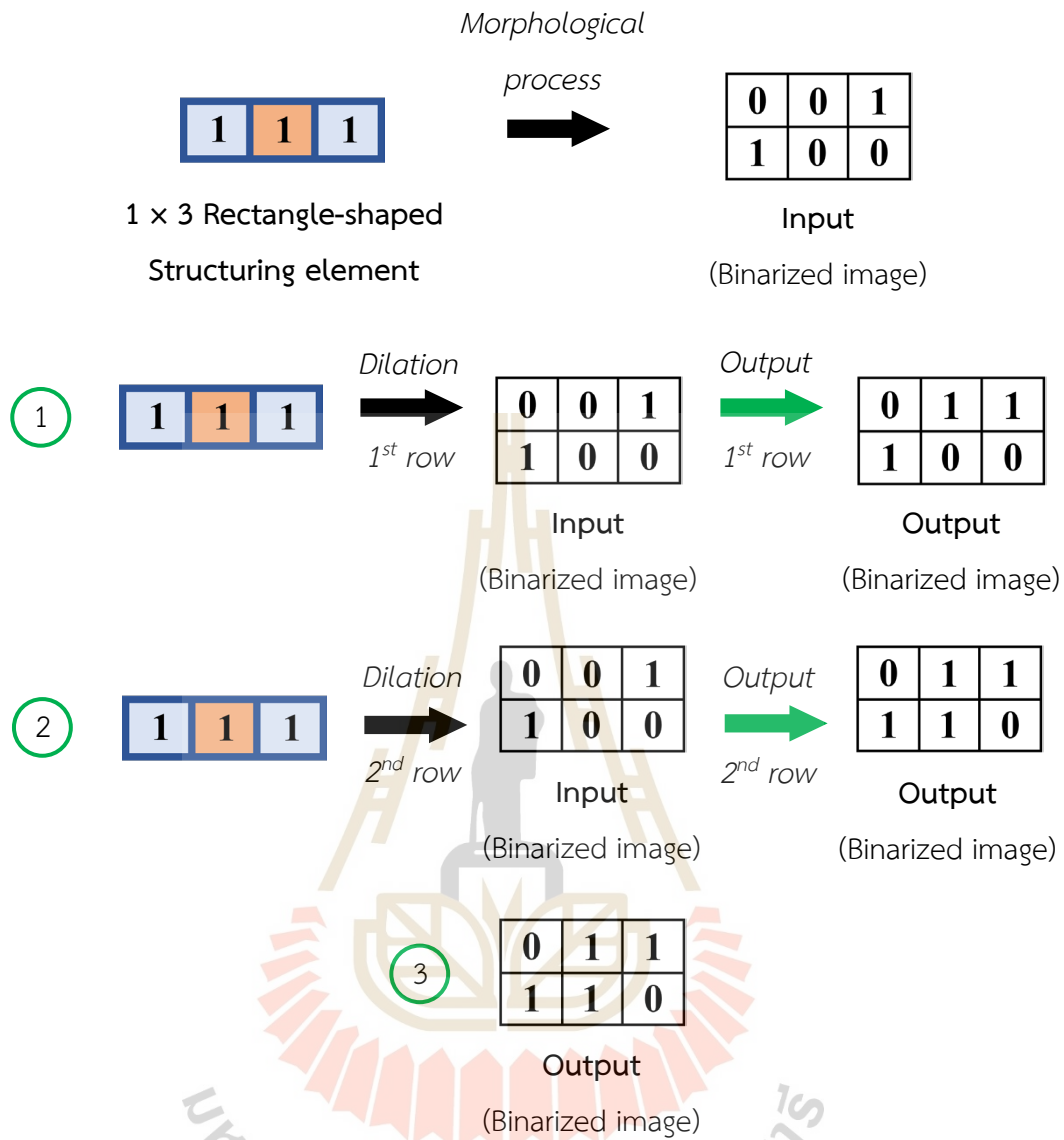


Figure 2.10 Block diagram of the dilation operation which increases the number of the white pixels of the binarized image.

Figure 2.10 shows the block diagram of the dilation operation with the 1 × 3 rectangle-shaped structuring element. The dilation operation is mathematically defined as (Moeslund, 2012)

$$g(x, y) = f(x, y) \oplus SE, \quad (2.7)$$

where $g(x, y)$ and $f(x, y)$ are the output and the input images, while SE represents the structuring element. In Eq. (2.7), the symbol \oplus denotes the dilation operation. Figure 2.10 illustrates the dilation operation of the 2×3 binarized image by the 1×3 rectangle-shaped structuring element. The orange color represents the origin of the structuring element. The dilation is done by superimposing the structuring element over the whole pixels of the binarized image. When any pixel in each superimposed area has the same value of 1, the value of the pixel image that aligns with the origin of the element is set to 1. Due to this operation, the pixel (1,2) of the output image has the value of 1 when the origin is aligned with it. After the dilation is applied to the first row, it is repeated to the next row. In the same fashion, the next pixel (2,2) becomes 1 in the next alignment of the origin. Finally, the dilated output image is obtained as shown in the figure in the third step.



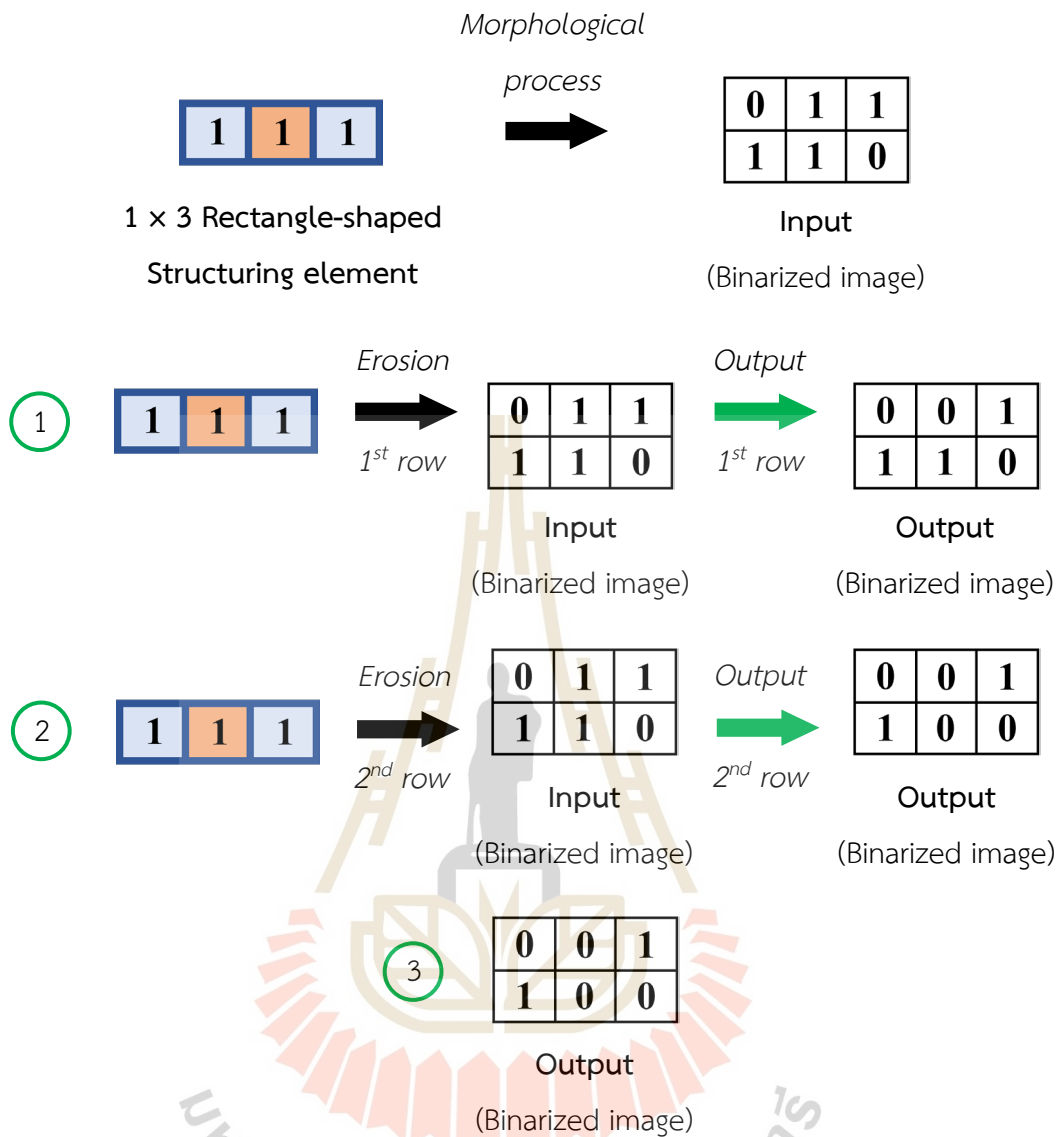


Figure 2.11 Block diagram of the erosion operation for reducing noise in the binarized image.

Figure 2.11 shows the block diagram of the erosion operation with the 1 × 3 rectangle-shaped structuring element. The erosion operation applied to the input image $f(x, y)$ by using the structuring element SE is defined as (Moeslund, 2012)

$$g(x, y) = f(x, y) \ominus SE, \quad (2.8)$$

where the \ominus denotes the erosion operation. The erosion of the binarized image by the

structuring element is done by the same superimposition operation. However, only when all pixels in the superimposed area have the same value as the structuring element, the value of the pixel image that aligns with the origin of the element is set to 1, otherwise is 0. Consequently, the pixels (1,2) and (2,2) are set to 0.

Although the morphological operation can increase or reduce the binarized image size, the type of the structuring element and its size should be selected according to the object shape. Figure 2.12(a) illustrates an input image extracted from a single video frame of a hand model in the RGB color. After converting the RGB color to the HSV color, the dilation operation thresholds the color, binarizing the input image. The resultant binarized image depicted in Figure 2.12(b) shows that not all pixels of the binarized hand image become white. The number of white pixels can be increased by using the disk-shaped structuring element with a radius of 3 as shown in Figure 2.12(c). However, although the number of white pixels increases, black pixels or holes still exist. This is because the size of the structuring element is not enough to increase the number of white pixels in the binarized hand image. Figure 2.12(d) shows the white hand image improved by using the structuring element with a radius of 7. Furthermore, the noise left in the binarized hand image is improved by using the Matlab function known as `imfill` to substitute the 0 value with 1.

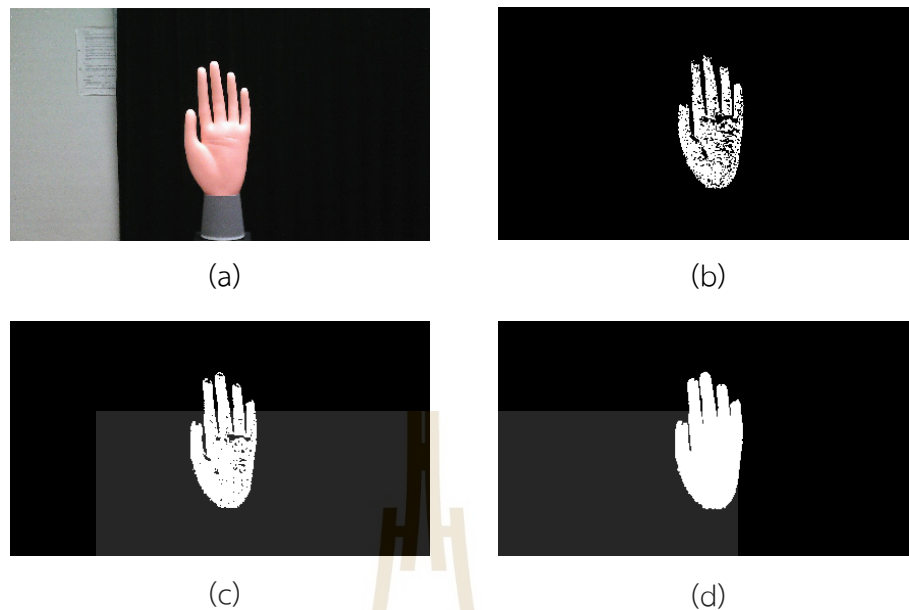


Figure 2.12 Morphological process of a color image. (a) The image of a hand model from a single video frame, (b) the resultant binarized image by thresholding the HSV color space. The dilated images using the disk-shaped structuring elements with a radius of (c) 3 and (d) 7.

2.4.3 Blob extraction

In computer vision, a blob is generally considered as a group of white pixels on a dark background. The blob extraction is the process of extracting the shape features of the white pixel region or the binarized image. In order to recognize the shape features, the blob extraction employs a 4-connectivity known as the Grass-fire algorithm.

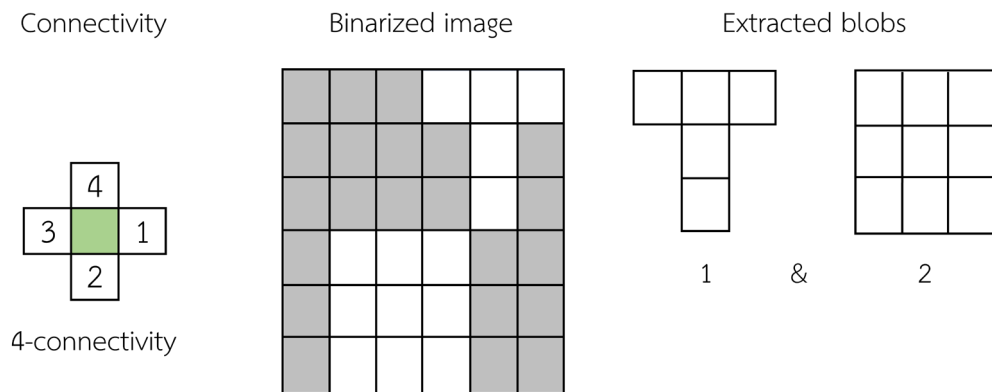


Figure 2.13 Result of applying the 4-connectivity in the binarized image (Moeslund, 2012).

Figure 2.13 shows the blob extraction of the binarized image by using the 4-connectivity. The green color area represents the origin of the connectivity that will not be included in the computation for extracting the blob. Blobs are extracted by using the Grass-fire algorithm. Figure 2.14 shows the operation of the Grass-fire algorithm for extracting the blob in the binarized input image by using 4-connectivity. There are four arms spread in four directions. The 4-connectivity can extract several blobs in the binarized image.

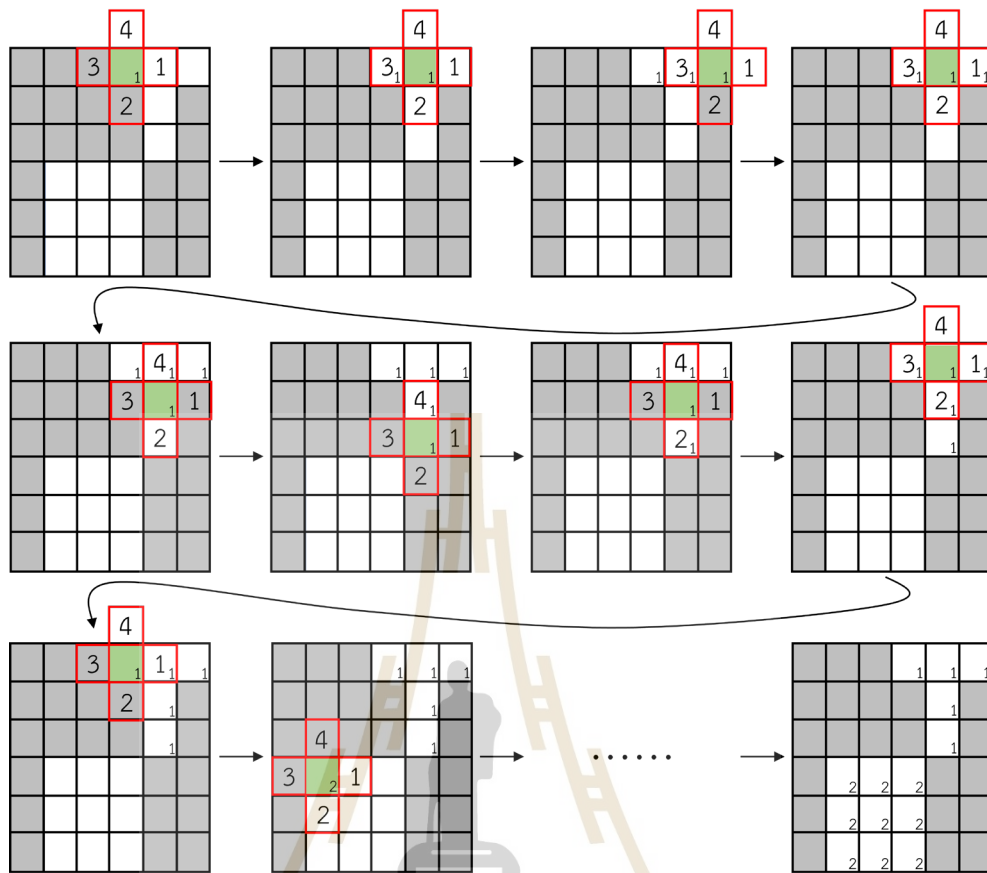


Figure 2.14 The Grass-fire algorithm for extracting the blobs in the binarized image (Moeslund, 2012).

The algorithm starts to superimpose the 4-connectivity pattern at the upper-left pixel of the binarized image. Consider the origin and the first arm of the connectivity align with the pixels at (4,1) and (5,1) in the input image. Since the input pixel (4,1) has the same value as the origin, the pixel (4,1) in the output image is set to have a value of 1 and then gives small labeling at the bottom-right corner of any white pixels. The small labeling indicates the number of the extracted blobs. According to the algorithm, the first arm detects the value of the superimposed pixel (5,1). Due to the matched value, the output pixel (5,1) is set to 1. Otherwise, it becomes 0. The second and the third arms perform the same value detections of the superimposed pixels. Next, the connectivity is shifted by 1 pixel, causing the alignments of the origin and the first arm with the pixels (5,1) and (6,1), respectively. The first arm detects the

value of the pixel (6,1), whether it is 1 or 0. In this superimposition, the input pixel (6,1) has a value of 1. Thus, the pixel of the output image is also set to 1. The blob extraction is then done for the next rows. As a result, the use of the 4-connectivity pattern gives two blobs as shown in the figure. After extracting the blob, the blob analysis calculates the blob area, centroid, and bounding box coordinates. The blob area calculates the number of white pixels in the blob. The centroid is the center of the blob mass, while the bounding box is the rectangle that confines the blob as shown in Figure 2.6. However, the blob analysis is dependent upon a clear foreground and background, light conditions, and the color of an object. Therefore, the color thresholding and the morphological operation are very important for performing correct hand detection.



CHAPTER III
RESEARCH METHODOLOGY

3.1 Proposed 3-D digital imaging system

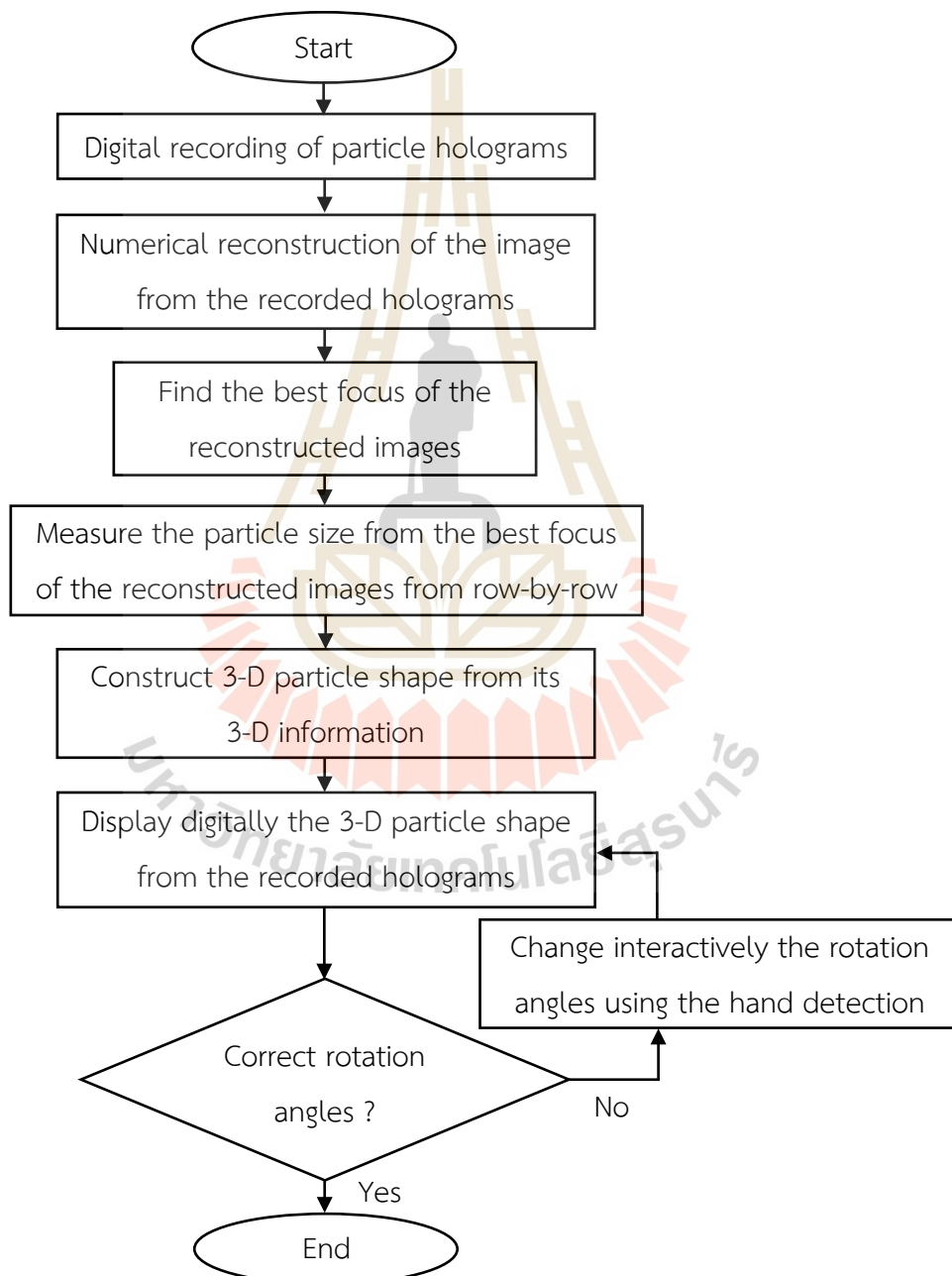


Figure 3.1 Flowchart for the interactive 3-D digital imaging system.

Figure 3.1 shows the flowchart of the 3-D digital imaging system. The proposed imaging system consists of two parts. The first part deals with the digital holographic recording and numerical reconstruction, while the second part is the interactive 3-D digital imaging. The first part can be described as follows: After recording the line-shaped particle as digital inline holograms using the CCD sensor, a set of the recorded particle holograms is numerically reconstructed from row-by-row using Fresnel diffraction integral at the different reconstruction distances. In order to find the best focus of the reconstructed images from row-by-row, the intensity sharpness of the reconstructed images is measured by using LAP. The particle diameter size is measured from the best focus of the reconstructed images row-by-row, while the particle depth position is given by its reconstruction distances. When the particle depth positions and their sizes are obtained from all rows of the holograms, the 3-D shape of the particle is digitally generated as a 3-D data array. For the experimental particle, this research proposed is studied by the line-shaped particle with orientation.

The second part displays the 3-D generated data of the particle holograms onto a computer monitor. The rotation angles of the digital 3-D imaging can be changed by detecting a hand movement via the webcam. As a result, 360-degree rotation angles of the 3-D generated data of the reconstructed particle can be digitally controlled and displayed onto a monitor, providing improved not only visual perception but also give the accuracy of morphological analysis.

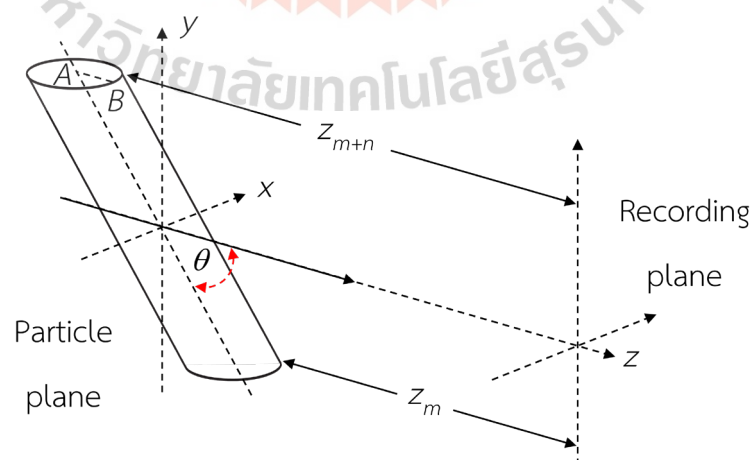
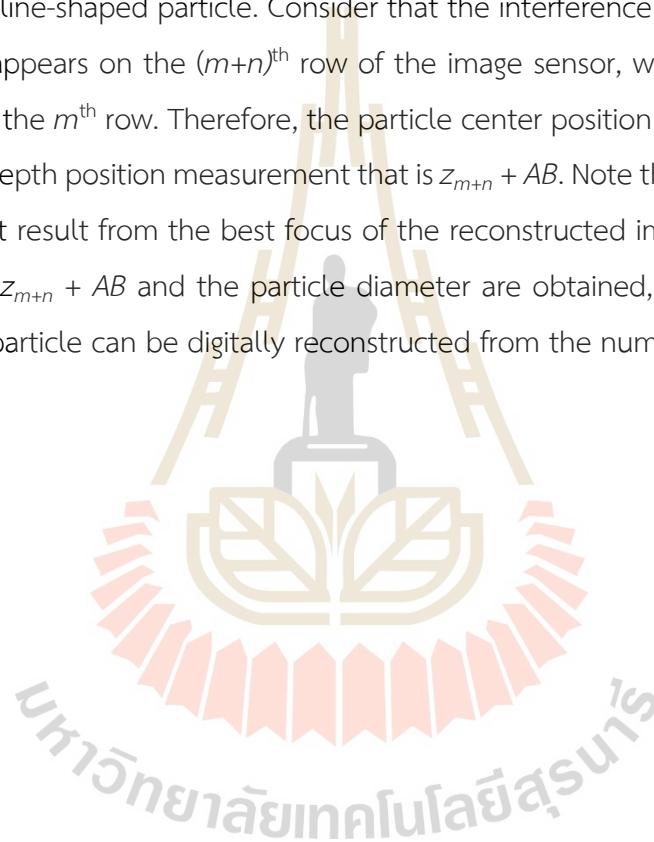


Figure 3.2 The orientation angle of the particle used in the hologram formation.

The feasibility of the proposed method is studied by imaging the 3-D line-shaped particle oriented in different angular directions θ . Figure 3.2 illustrates a schematic diagram of the experimental line-shaped particle orientation, which makes an angle θ with respect to the z-axis. Since the experimental line-shaped particle has the orientation angles, the intensity transmittance of the particle hologram in each row that was recorded onto the CCD sensor will have different recording distances.

Point A lies on the axis of a 2-D circle with the orientation angle θ . AB is the radius of the line-shaped particle. Consider that the interference fringe from the top of the particle appears on the $(m+n)^{\text{th}}$ row of the image sensor, while the one from the bottom is on the m^{th} row. Therefore, the particle center position can be obtained from the particle depth position measurement that is $z_{m+n} + AB$. Note that z_{m+n} is the distance measurement result from the best focus of the reconstructed image. Therefore, when the distance $z_{m+n} + AB$ and the particle diameter are obtained, the 3-D shape of the line-shaped particle can be digitally reconstructed from the numerical reconstructions.



3.2 Numerical reconstructions of particle holograms

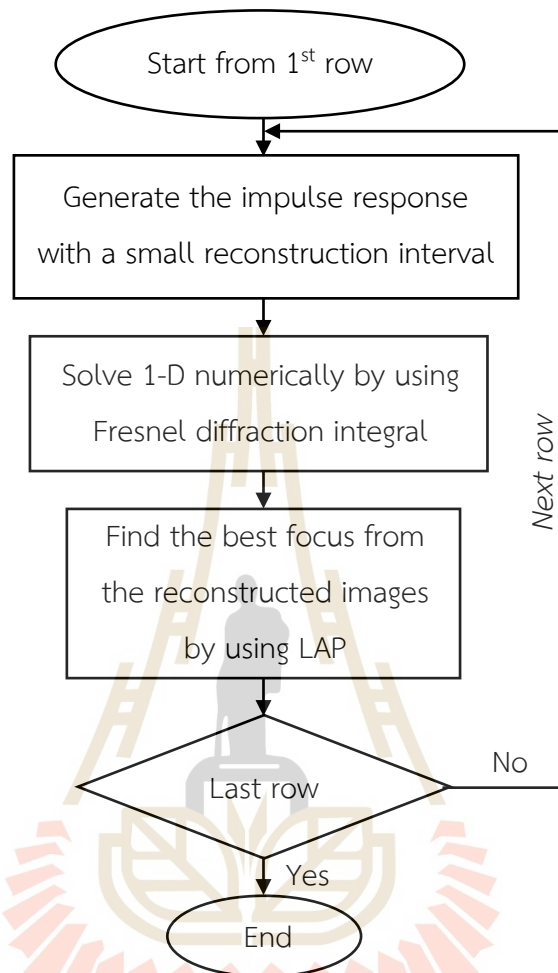


Figure 3.3 Flowchart for the numerical reconstruction of the particle holograms.

Figure 3.3 shows the flowchart for the numerical reconstruction of the particle holograms row-by-row by using the Fresnel diffraction integral. The numerical reconstruction process starts from the 1st row of the recorded holograms. After the numerical reconstructions, the correct depth position of the particle is searched by finding the best focus of the reconstructed images via the LAP operation. The numerical reconstructions are done until the last row.

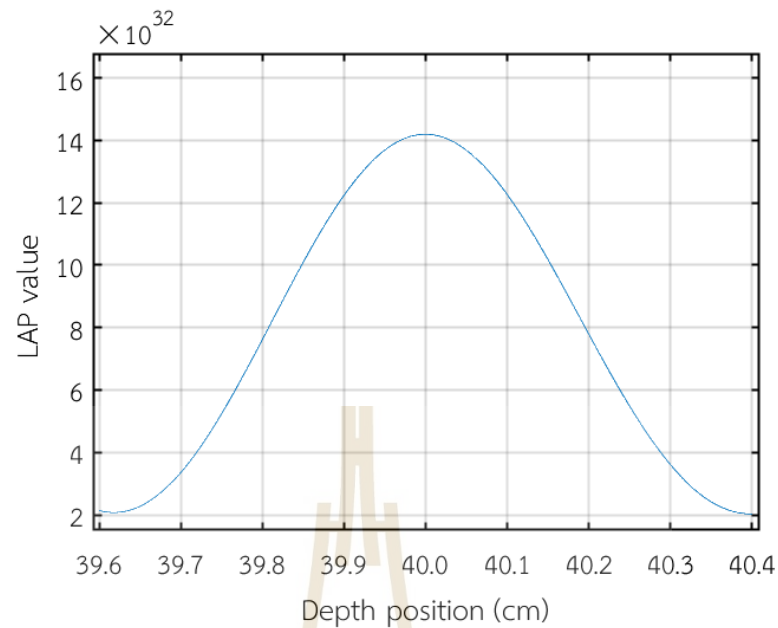


Figure 3.4 The LAP calculation from the Fresnel-based numerical reconstructions of the line-shaped particle hologram simulated at the recording distance $z = 40$ cm.

Figure 3.4 shows the LAP calculation result from the Fresnel-based numerical reconstructions of the simulated particle hologram as a function of the reconstruction distances. The reconstructions were done between 39.6 – 40.4 cm with a reconstruction interval of 2.5 μm . The LAP gives the maximum output value at the one correct depth position, which is 40.0 cm. In this research work, the particle depth position recorded in each row varies, therefore, the LAP has to be repeatedly used to locate different depth positions from each row. Finally, when the correct depth position of the particle is found, the depth is used to reconstruct the particle image in order to extract the diameter information.

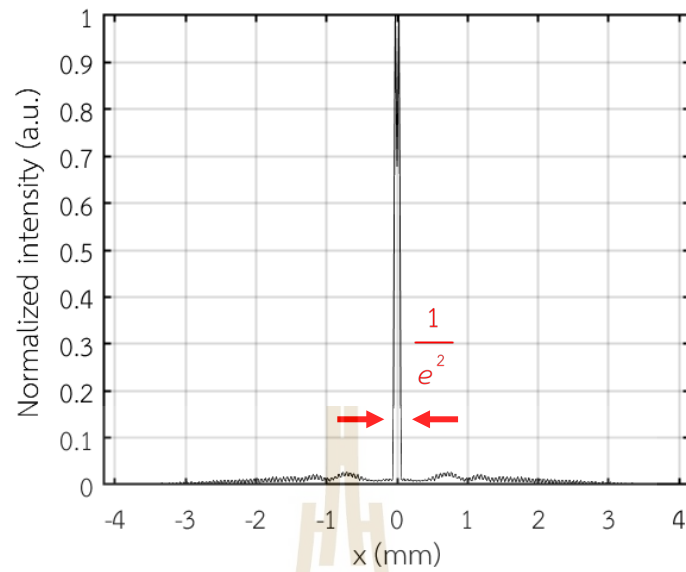


Figure 3.5 Normalized numerical reconstruction image of the line-shaped particle hologram.

Figure 3.5 shows the normalized 1-D numerical reconstruction of the simulated hologram of the 100 μm line-shaped particle with the background removal. The particle diameter can be measured from the width of the normalized image reconstruction at $\frac{1}{e^2}$ of its maximum intensity.

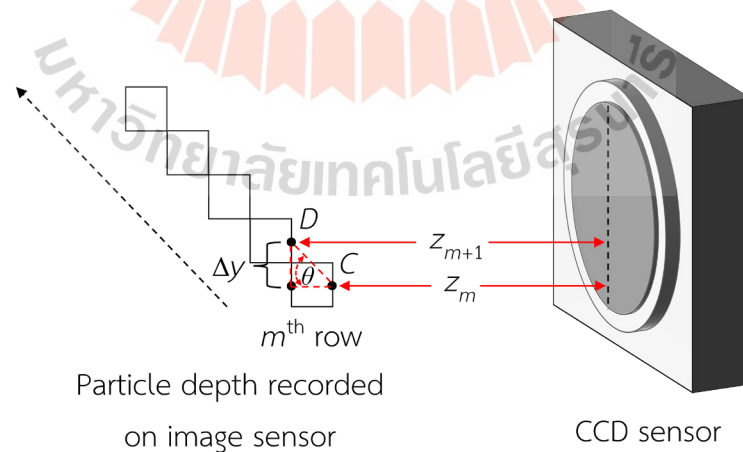


Figure 3.6 Geometry relationship between the particle depth, orientation angle and the array image sensor.

Figure 3.6 illustrates a schematic diagram of the geometrical relationship between the particle depth z , orientation angle θ , and the sensor pixel position during the hologram recording. Consider that the interference fringes with the distances z_m and z_{m+1} away from the sensor are recorded along the m^{th} and the $(m+1)^{\text{th}}$ rows, respectively. The particle orientation angle can be calculated by using the difference between the particle depths from two adjacent rows as

$$\tan \theta = \frac{\text{Pixel size } \Delta y}{z_{m+1} - z_m} \quad (3.1)$$

Eq. (3.1) is useful for obtaining the average orientation of the whole particle length.



3.3 Formation of 3-D line-shaped particle

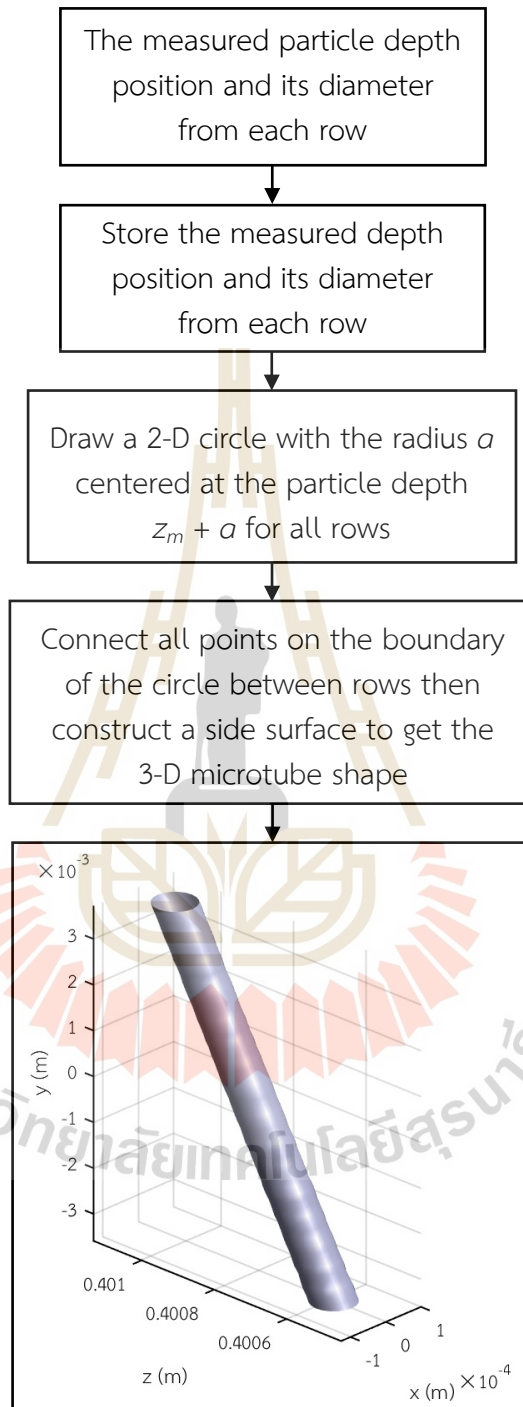


Figure 3.7 Flowchart for displaying the 3-D line-shaped particle from the numerical reconstruction results.

Figure 3.7 shows the flowchart for displaying the 3-D line-shaped particle from the numerical reconstruction results. To form the 3-D line-shaped particle, the proposed method utilizes the measured particle depth position and its diameter to draw circles in each row. The center of the circle is determined from the summation of the particle depth z_m and the particle radius a .

After drawing the 2-D circle for every row, a side surface is constructed by connecting all points of the 2-D circle between rows.

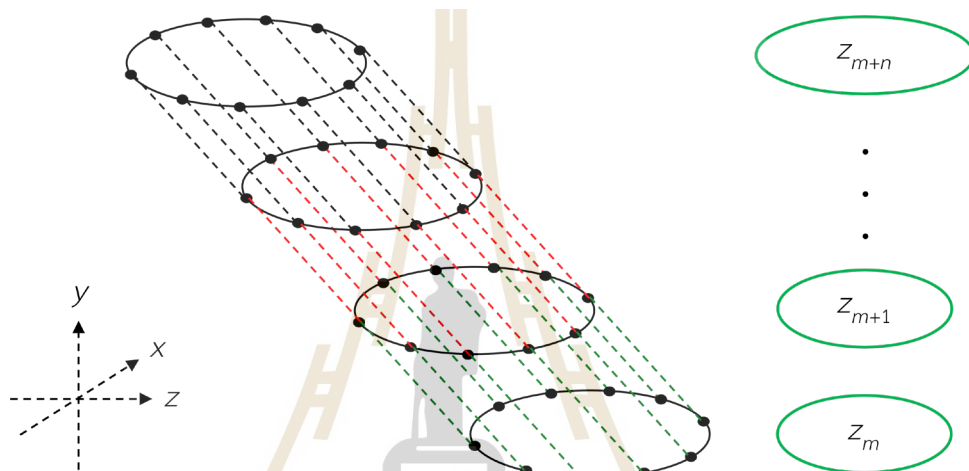


Figure 3.8 Construction of the particle side surface by connecting all points on the 2-D circle between rows.

Figure 3.8 illustrates constructions of the particle side surface by connecting all points on the 2-D circle between the rows $z_m, z_{m+1}, \dots, z_{m+n}$. In this research work, the (x, y) coordinate points on each 2-D circle are set to only 20 points to save computation time. As a result, the 3-D line-shaped particle can be digitally constructed.

3.4 Interactive imaging system

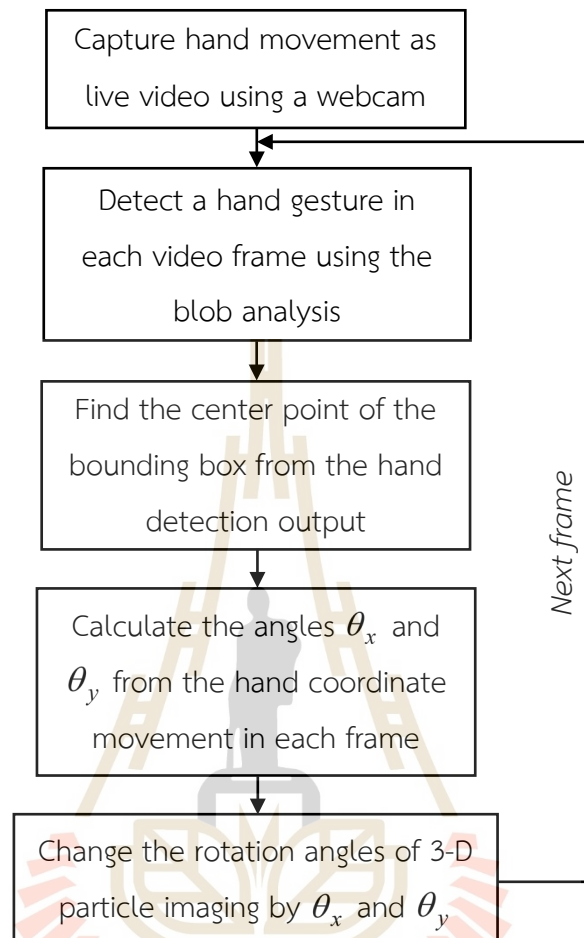


Figure 3.9 Flowchart for the interactive 3-D particle imaging.

Figure 3.9 shows the flowchart for the interactive 3-D particle imaging by using the hand detection. When a user's hand appears in front of the webcam, the hand detection program starts to record a live video of the movements. An image sequence frame-by-frame of the video is generated and then analyzed using the blob analysis, providing the information of the coordinate (x_p, y_p) at the upper-left corner and the center point (x_{center}, y_{center}) of the bounding box. They are related as

$$x_{center} = x_p + \frac{width_{bb}}{2} \quad (3.2)$$

and

$$y_{center} = y_p + \frac{height_{bb}}{2}, \quad (3.3)$$

where $width_{bb}$, and $height_{bb}$ are the width and the height of the bounding box. In order to implement the proposed interactive imaging, the hand movement coordinate (d_x, d_y) is converted into a rotation angle of the displayed particle image from the holograms. The coordinate (d_x, d_y) is measured with respect to the center of the bounding box.

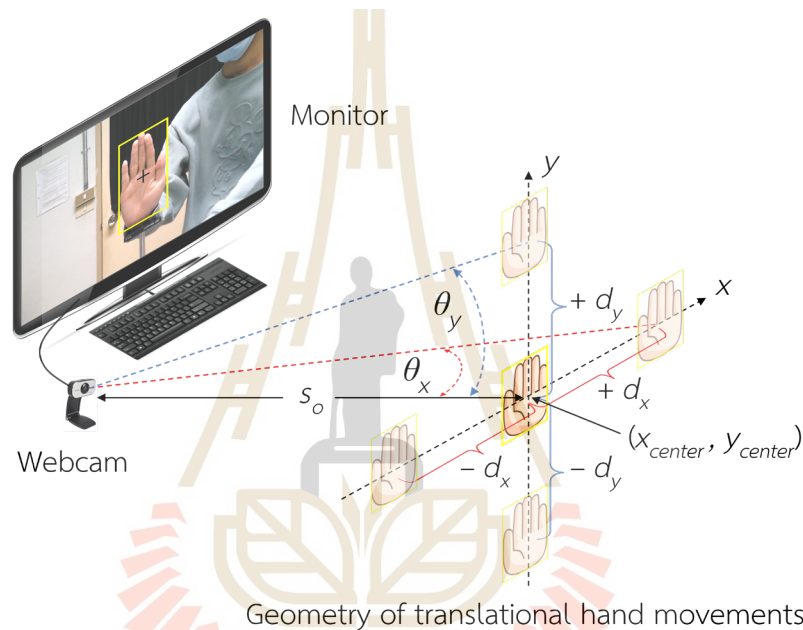


Figure 3.10 Schematic diagram of translational hand movements.

Figure 3.10 shows a schematic diagram of the hand detection setup by using the webcam connected to a computer system. The array image sensor is located at the distance s_i behind the lens. A user's hand palm with a height h_o is located at the predefined xy plane with the distance s_o away from the sensor center. According to the lens equation (Pedrotti *et al.*, 2012), the palm height h_o is related to the image height h_i captured by the webcam sensor by

$$h_o = \frac{h_i \times s_o}{s_i}. \quad (3.4)$$

Consider that the hand palm translates in the xy plane to the coordinate (d_x, d_y) and is detected by using the proposed method. If the blob analysis of a single frame provides a new center of the bounding box at the coordinate (c_x, c_y) in the image plane, the hand movement coordinate can be defined as

$$d_x = \frac{(\text{Webcam center} - c_x) \times \text{pixel size of webcam} \times s_o}{s_i}, \quad (3.5)$$

and

$$d_y = \frac{(\text{Webcam center} - c_y) \times \text{pixel size of webcam} \times s_o}{s_i}. \quad (3.6)$$

The proposed interactive imaging converts the hand movement into a rotation angle of the displayed particle image as

$$\theta_x = \arctan\left(\frac{d_x}{s_o}\right) \quad (3.7)$$

and

$$\theta_y = \arctan\left(\frac{d_y}{s_o}\right), \quad (3.8)$$

respectively. The angles θ_x and θ_y become bigger when the hand movement distance increases.

3.5 Rotation angles of 3-D particle imaging

In the proposed method, the calculated angles θ_x and θ_y are employed for interactively rotating the orientation of the reconstructed 3-D particle.

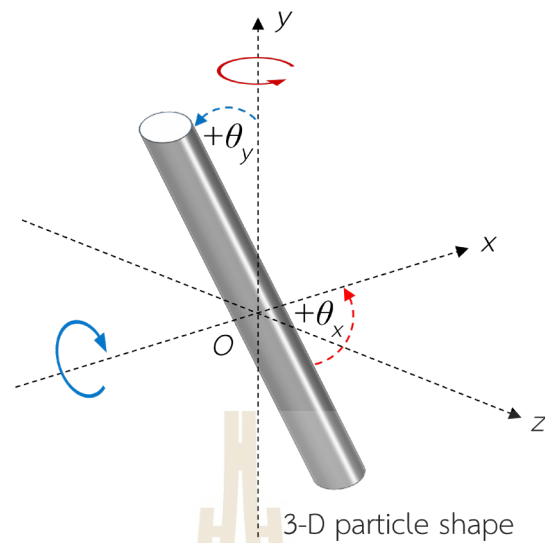


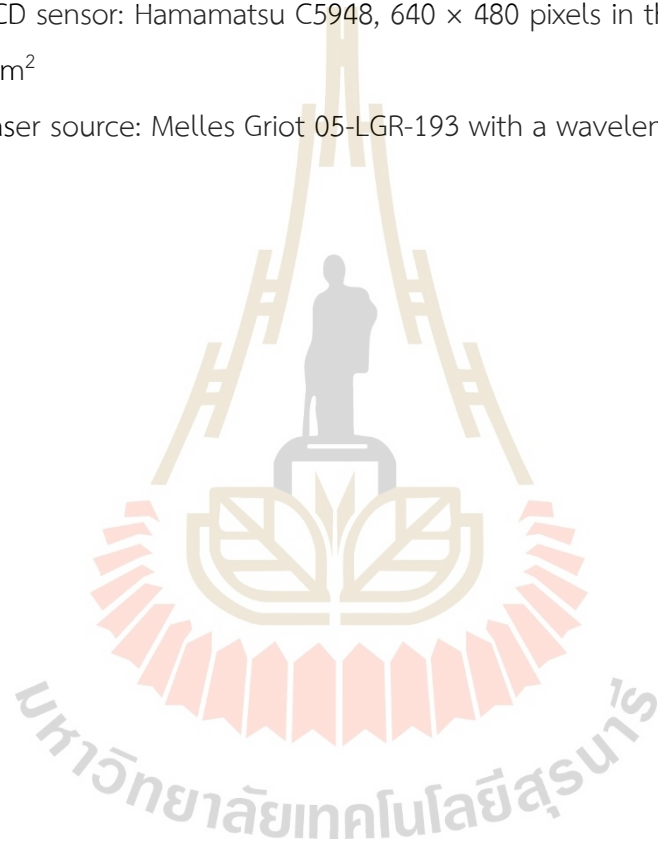
Figure 3.11 Rotation direction of the reconstructed 3-D particle by using the rotate function in Matlab.

In Matlab, the rotate function is used to rotate an object orientation around any axis of the Cartesian coordinate system. The rotate function transforms the coordinate of the 3-D object $[x_{object}, y_{object}, z_{object}]$ with respect to the origin. In this work, the origin is defined at the 240th row. Figure 3.11 illustrates the rotation direction by using the rotate function. The blue and the red arrows represent the rotation directions around the x- and the y-axes, respectively. The rotation around the x-axis can be considered as the rotation with respect to the y-axis by the angle θ_y , while the rotation around the y-axis is equal to the rotation with respect to the x-axis by the angle θ_x .

In the proposed method, the 3-D particle imaging reconstructed from the digital holograms can be interactively controlled by the translational movements of the hand in the xy plane using hand detection that is captured via an external webcam as a live video. The hand movements in the positive axes correspond to positive angles θ_x and θ_y , otherwise, are negative angles θ_x and θ_y . When a user's hand moves along the positive x-axis, the original 3-D particle will be rotated with respect to the x-axis by the angle $+\theta_x$ as shown in the figure. In the case of the hand moves along the positive y-axis, the 3-D particle will be rotated with respect to the y-axis according to the angle $+\theta_y$. Otherwise, the 3-D particle will rotate in the opposite direction as described above.

3.6 Instrumentations

1. Notebook computer: Asus A540U, Intel i7 7500U, 12 GB of Ram and Intel(R) HD Graphic 620
2. Webcam: OKER (386), 1920 × 1080 pixels with 2.797 μm pixels size
3. Software: Matlab 2019b
4. Line-shaped particle: A microtube (Polycarbonate Capillary Tubing / Paradigm Optics) with a diameter of 100 μm
5. CCD sensor: Hamamatsu C5948, 640 × 480 pixels in the area of 8.30 × 6.40 mm^2
6. Laser source: Melles Griot 05-LGR-193 with a wavelength of 543.5 nm



CHAPTER IV

EXPERIMENTAL VERIFICATIONS

In this chapter, the information of the line-shaped particle, which are the particle depth, size, and orientation angles, will be experimentally measured. The next verification is the hand movement detected by using the blob analysis, which will be used for changing the extracted particle orientation in order to facilitate the proposed 3-D morphological analysis. Finally, the interactive imaging of the 3-D microtube reconstructed from the digital particle holograms will be discussed. All computations in the proposed method were done by using Matlab 2019b, which run on Windows 10.

4.1 Experimental information extraction from the particle holograms

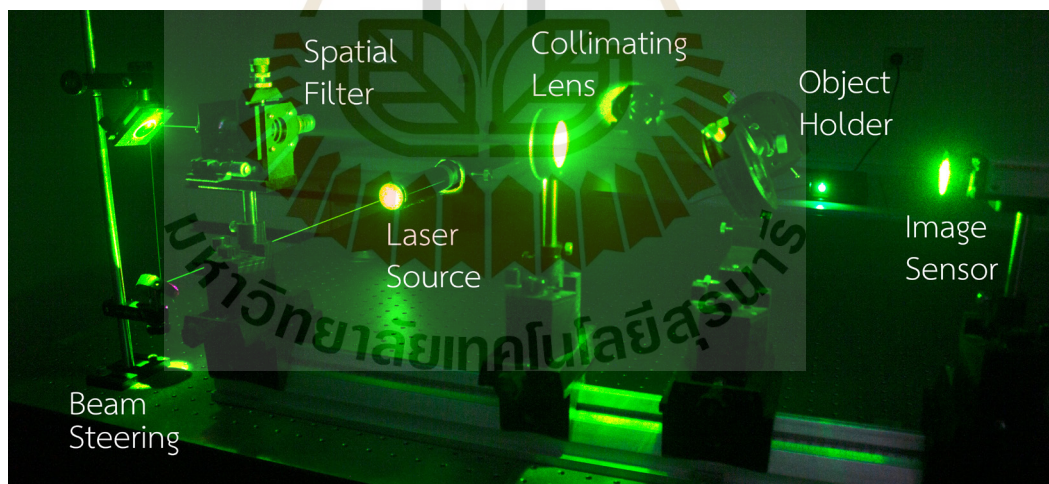


Figure 4.1 Experimental setup for recording the line-shaped particle holograms.

Figure 4.1 shows a schematic diagram of the experimental setup for digitally recording the line-shaped particle holograms. The monochromatic light wave generated from the laser source with the wavelength λ of 543.5 nm (Melles Griot, 05-LGR-193)

was used to illuminate the 100 μm polycarbonate microtube (Paradigm Optics, CTPC-067-100) placed on a rotational object holder. The particle orientation angles were set to 60° and 75° with respect to the setup optical axis. The particle holograms were recorded at the recording distances z of 34, 36, 38, and 40 cm by using the CCD sensor (Hamamatsu, C5948) with the resolution of 640×480 pixels in the area of 8.30×6.40 mm^2 . Due to the orientation angle, each row of the recorded hologram will have a different recording distance.

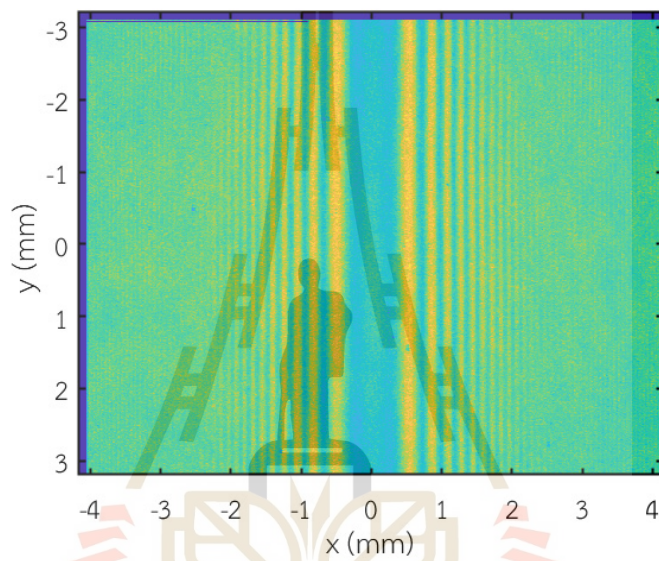


Figure 4.2 The experimentally recorded digital inline hologram of the 100 μm line-shaped particle at the recording distance z of 40 cm with the angle θ of 60° .

Figure 4.2 shows the experimentally recorded digital inline hologram of the 100 μm line-shaped particle, which was recorded with the angle $\theta = 60^\circ$ at the recording distance z of 40 cm. The hologram picture was plotted by using Matlab function known as `imagesc`. This function vertically flips the scale axis. Consequently, the top part of the picture corresponds to the bottom particle and has a small row number, while the bottom picture displays information related to the top particle and has a large row number. This is caused by the different recording distance z in each row along the y -axis. The black areas on the top and left are dead pixels of the sensor. They appear in the first eleven rows and columns.

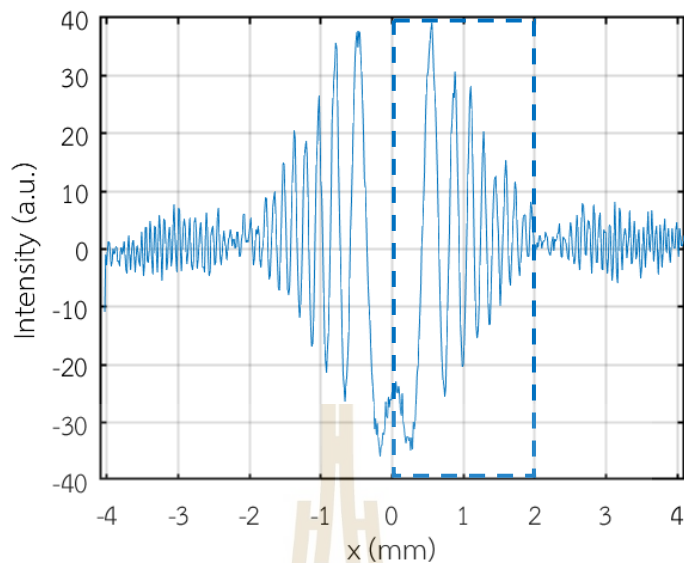


Figure 4.3 1-D intensity transmittance of the experimental hologram shown in Figure 4.2 scanned along the horizontal axis at $y = 20^{\text{th}}$ row.

Figure 4.3 shows a 1-D intensity transmittance of the particle hologram shown in Figure 4.2 scanned along the horizontal axis at $y = 20^{\text{th}}$ row corresponding to the bottom particle. The $+1^{\text{st}}$ minimum of the envelope appears around the position $x = 2$ mm. In Figure 4.4, the intensity transmittance corresponding to the top particle is scanned along the 480^{th} row. The $+1^{\text{st}}$ minimum appears around the position $x = 3$ mm. According to Eq. (2.1), the minimum position difference is caused by the fact that the width of the sinc function is proportional to $\lambda z/a$. Since the recording distance z at the row $y = 20^{\text{th}}$ row is shorter than that of $y = 480^{\text{th}}$ row, the width of the envelope function shown in Figure 4.3 is narrower than that in Figure 4.4. Note that for computational purposes, the background signals in Figures 4.3 and 4.4 were removed by subtracting the background intensity from the hologram.

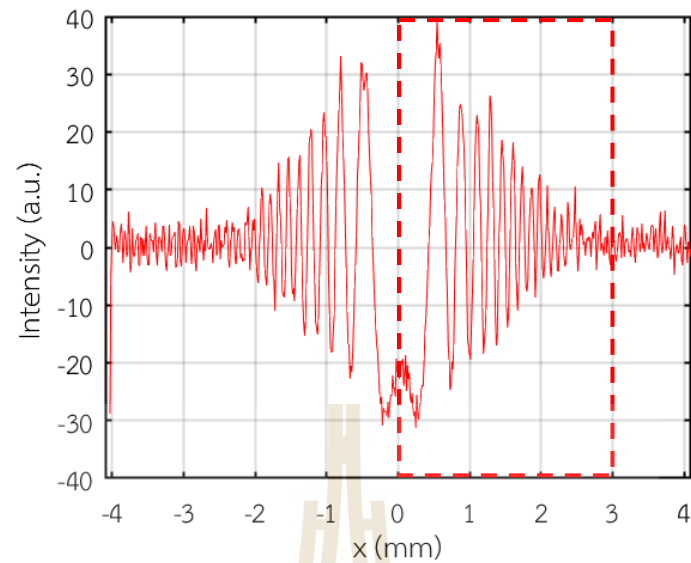


Figure 4.4 1-D intensity transmittance of the experimental hologram shown in Figure 4.2 scanned along the horizontal axis at $y = 480^{\text{th}}$ row.

4.2 Particle depth measurement

In order to measure the particle depth from each row, the Fresnel diffraction integral is used for numerically reconstructing a set of particle images from the holograms at different reconstruction distances. To determine the correct particle depth, the sharpness of the numerically reconstructed images is measured by using the LAP operation. The LAP gives the maximum output value when the image reconstructed at the correct depth position has the highest sharpness.

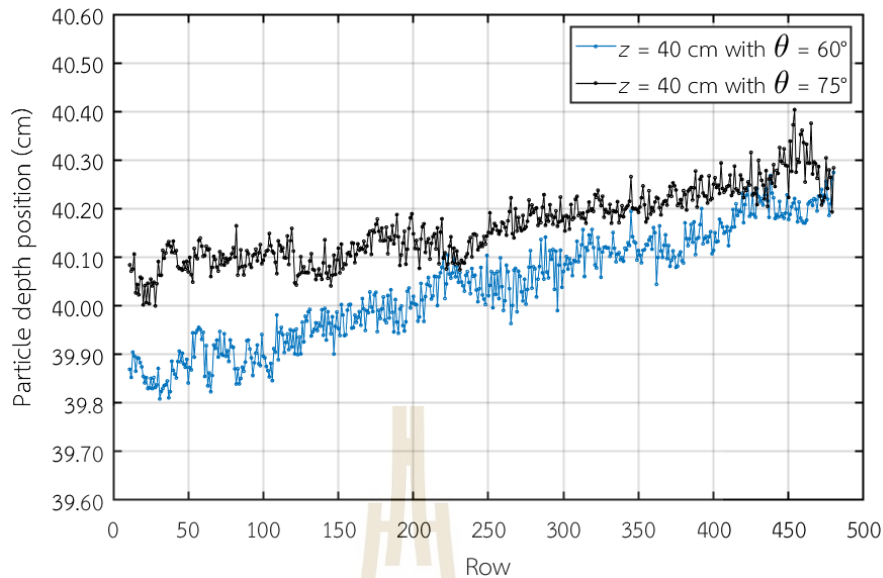


Figure 4.5 The depth measurements of the 100 μm microtube at the recording distance $z = 40$ cm with the angles $\theta = 60^\circ$ and 75° .

Since the first 10 rows along the horizontal axis consist of dead pixels as shown in Figure 4.2, the numerical reconstruction was done from the 11th until the 480th row, giving the total number of rows of 470. A set of the impulse responses of a free space propagation with the reconstruction distance interval of 2.5 μm was generated to solve the Fresnel diffraction integral for each row. After measuring the sharpness of the reconstructed image of each row, the LAP gave a single maximum value that corresponds to the correct depth position of the microtube. Figure 4.5 plots the whole particle depth measurements of the hologram recorded at the distance $z = 40$ cm with the angles $\theta = 60^\circ$ and 75° . The results show that the bigger the particle orientation angle, the higher the slope of the plotted depth. They agree well with the real particle orientation during the hologram recordings, where the recording distance of the top particle was longer than that of the bottom.

Figure 4.6 shows the depth measurements of the 100 μm microtube at the recording distance $z = 34$ cm with the orientation angles $\theta = 60^\circ$ and 75° as a function of the rows. A similar trend of the depth variations is obtained for the holograms recorded at different distances.

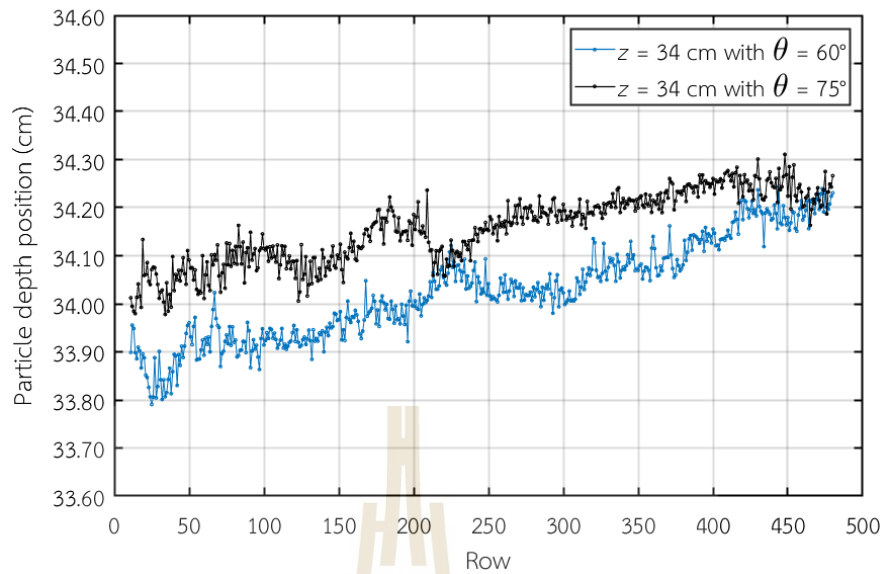


Figure 4.6 The depth measurements of the 100 μm microtube at the recording distance $z = 34$ cm with the angles $\theta = 60^\circ$ and 75° .

Figures 4.5 and 4.6 show that there are errors in the measurement of the particle depths. Table 4.1 shows the mean absolute percentage errors (MAPE) in the depth measurement of the 100 μm microtube at the recording distances $z = 34, 36, 38,$ and 40 cm with the orientation angles $\theta = 60^\circ$ and 75° . The mean absolute percentage errors were calculated from the 470 errors in the depth measurements. It is apparent that the errors are larger for the shorter recording distances z than the longer distance. This is because the spatial frequency of the chirp signal for the shorter recording distance z is higher, causing a stronger aliasing effect. Therefore, this is important to use a higher resolution of the image sensor for recording the particle hologram. Furthermore, the measurement errors of a larger orientation angle $\theta = 75^\circ$ are higher than the smaller angle. This may be caused by the larger orientation angle having a smaller change in the depth position between two adjacent rows compared with the smaller angle. The reconstruction interval of $2.5 \mu\text{m}$ may not be fine enough for locating the particle depth position.

Table 4.1 Mean absolute percentage errors in the depth measurements of the line-shaped particle.

Recording distance z (cm)	MAPE in the depth measurements (%)	
	Orientation angle $\theta = 60^\circ$	Orientation angle $\theta = 75^\circ$
40.0	0.0815	0.336
38.0	0.118	0.570
36.0	0.126	0.348
34.0	0.148	0.364

4.3 Particle orientation measurement

In the proposed method, the orientation angle of the particle shown in Figure 3.6 can be measured by using the relationship between the sensor pixel size Δy and the difference of the measured depth position Δz between two adjacent rows that is $\theta = \arctan(\Delta y/\Delta z)$. Table 4.2 shows the mean absolute percentage errors in the orientation angle measurement of the 100 μm microtube at the recording distances z of 34, 36, 38, and 40 cm with the orientation angles $\theta = 60^\circ$ and 75° . The average measured orientation angles of the whole line-shaped particle were obtained by calculating Eq. (3.1). In comparison with Table 4.1, a similar trend of the measurement errors is obtained for the shorter recording distance and the larger orientation angle.

Table 4.2 Mean absolute percentage errors in the orientation angle measurements of the line-shaped particle.

Recording distance z (cm)	Mean calculated orientation angle ($^\circ$)		MAPE in the orientation angle measurements (%)	
	$\theta = 60^\circ$	$\theta = 75^\circ$	$\theta = 60^\circ$	$\theta = 75^\circ$
	40.0	59.9	74.3	0.167
38.0	59.7	74.1	0.500	1.20
36.0	59.4	73.6	1.00	1.87
34.0	59.1	73.2	1.50	2.40

4.4 Particle size measurement

The particle diameter was measured from the best focus of the numerical reconstructed particle image in each row. After normalizing the best focus image intensity, the microtube diameter was measured at $1/e^2$ of the maximum normalized intensity from each row as shown in Figure 3.5.

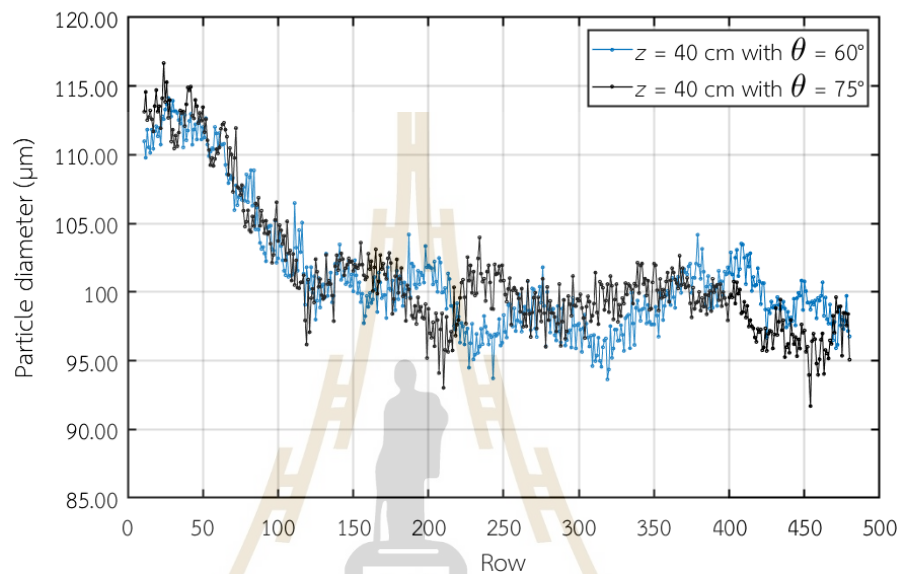


Figure 4.7 The particle diameter measurements of the 100 μm microtube at the recording distance $z = 40$ cm with the angles θ of 60° and 75° .

Figure 4.7 plots the diameter measurements of the 100 μm microtube at the recording distance z of 40 cm with the orientation angles $\theta = 60^\circ$ and 75° as a function of the rows. As a result, the first measured 100 rows have a larger diameter than the others because they have the shorter depth position of the microtube corresponding to the orientation angle of the particle. The effect of the depth position on the measurement accuracy is similar to those represented in Tables 4.1 and 4.2. They are related to the high spatial frequency of the chirp signal. The aliasing effect is higher at the closer depth position than that at the longer depth position.

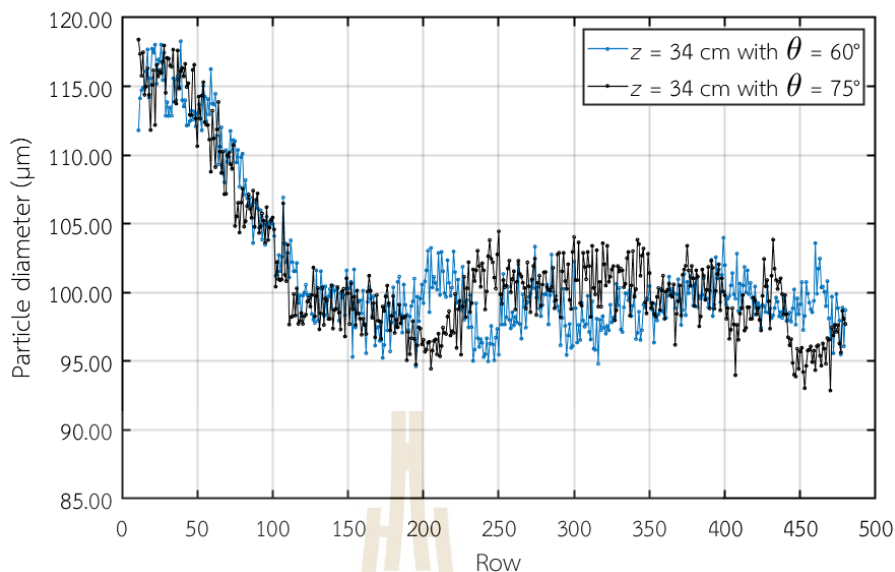


Figure 4.8 The particle diameter measurements of the 100 μm microtube at the recording distance $z = 34$ cm with the angles θ of 60° and 75° .

To verify this sampling effect, Figure 4.8 shows the particle diameter measurements of the 100 μm microtube at the recording distance z of 34 cm with the orientation angles $\theta = 60^\circ$ and 75° . Similar measurement results are obtained in the shorter recording distance shown in Figure 4.8.

Table 4.3 Mean absolute percentage errors in the diameter measurements of the line-shaped particle.

Recording distance z (cm)	Mean calculated diameter (μm)		MAPE in the diameter measurements (%)	
	$\theta = 60^\circ$	$\theta = 75^\circ$	$\theta = 60^\circ$	$\theta = 75^\circ$
40.0	101.24	101.41	1.24	1.41
38.0	101.48	101.43	1.48	1.43
36.0	101.55	101.52	1.55	1.52
34.0	101.58	101.64	1.58	1.64

Table 4.3 shows the mean absolute percentage errors in the diameter measurement of the 100 μm microtube at the recording distances z of 34, 36, 38, and

40 cm with the orientation angles $\theta = 60^\circ$ and 75° . Due to the dependency of the particle diameter measurement upon the depth measurement, the mean absolute percentage errors in Table 4.3 becomes higher as the recording distance z is shorter and the orientation angle is bigger.

4.5 3-D Display of the particle image

4.5.1 Particle image with non-uniform surface

The extracted particle depths and diameters can be used to display the 3-D shape of the microtube digitally according to the proposed described in Sect. 3.3. For each row, the center of the microtube was located by using the measured depth, then the 2-D circles were drawn at the different centers for 470 rows. Finally, the side surface of the 3-D microtube was constructed by connecting all points on the 2-D circle between two adjacent rows.

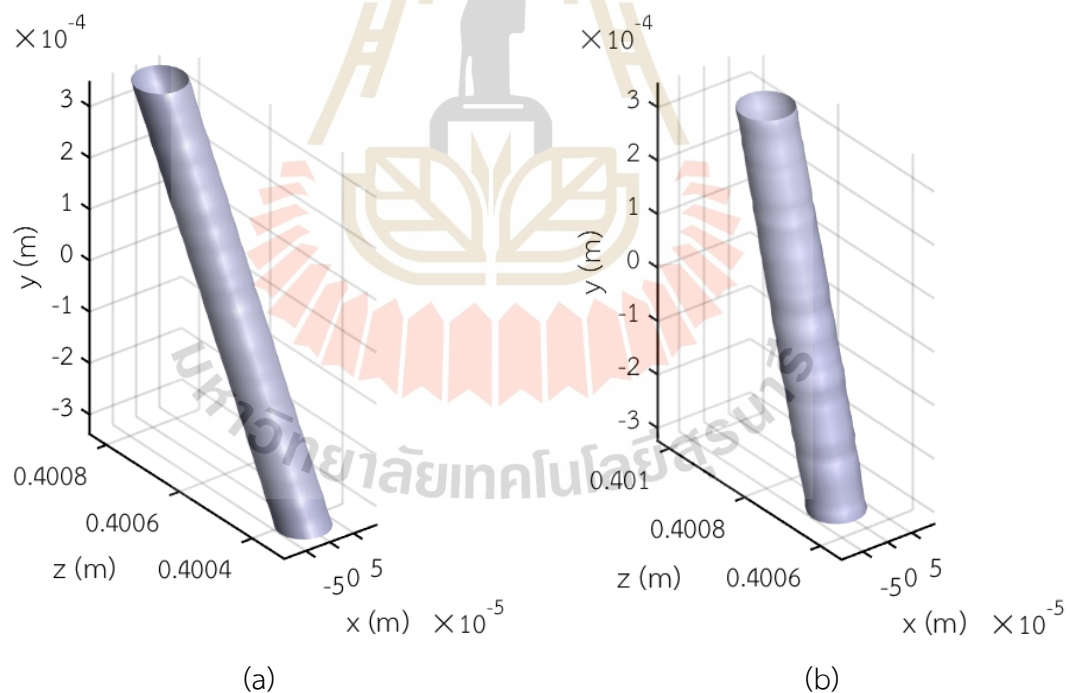


Figure 4.9 3-D display of the microtube shape at the recording distance $z = 40$ cm with the orientation angles θ (a) 60° and (b) 75° .

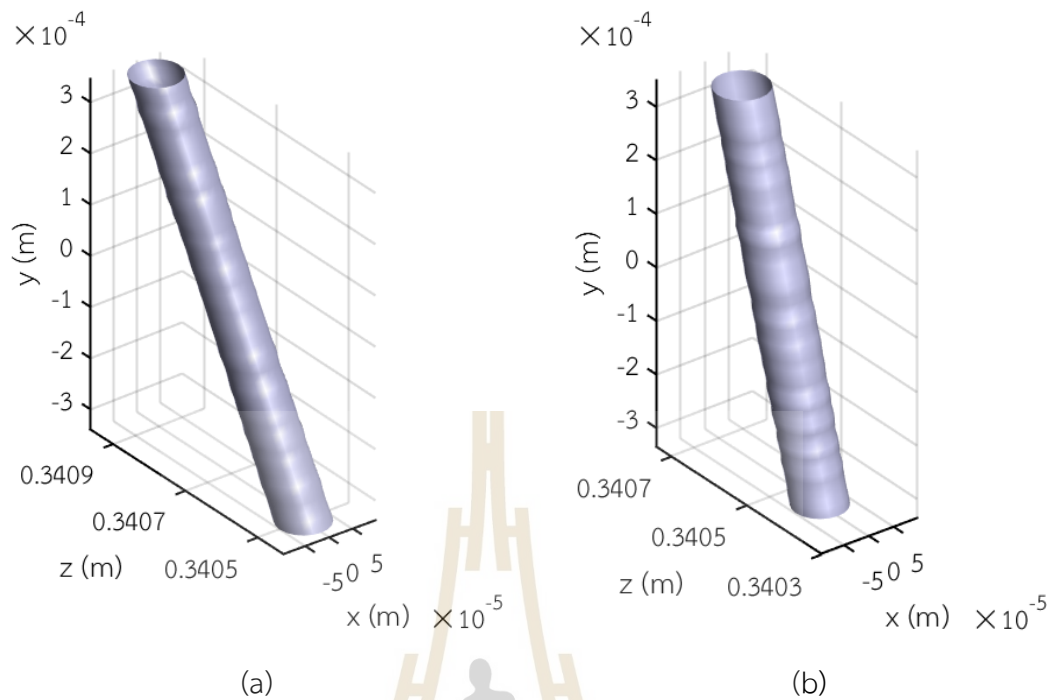


Figure 4.10 3-D display of the microtube shape at the recording distance $z = 34$ cm with the orientation angles θ (a) 60° and (b) 75° .

Figures 4.9 and 4.10 show the 3-D displays of the microtube shape at the recording distances $z = 40$ cm and 34 cm with the orientation angles $\theta = 60^\circ$ and 75° . They were plotted by using the measured particle depth and size from each row. In the figure, the y -axis and z -axis correspond to the row or the vertical axis of the image sensor and the depth position, respectively. In the figure, the z -axis was plotted as a function of the measured separation distance between the particle and the sensor. It agrees with the recording setup where the top particle had a longer separation than the bottom. The 3-D microtube shape is constructed from the row with the smallest depth measurement error. The depth positions in other rows were calculated from the two adjacent rows according to $\Delta z = \Delta y / \tan(\theta_m)$, where θ_m is the mean measured rotation angle presented in Table 4.2. It is clear from Figures 4.9 and 4.10 that the 3-D microtube shapes have non-uniform surfaces. This was caused by the errors in the diameter measurements. As a result, the reconstruction of the side surface with the orientation angle $\theta = 75^\circ$ has bigger non-uniformity compared with that of the orientation angle $\theta = 60^\circ$.

4.5.2 Changes of Particle Image Orientation

In this work, the orientation angle of the 3-D particle image will be changed according to the hand gesture detected by the webcam. The particle orientation change will be implemented by using Matlab function known as rotate. Figures 4.11 and 4.12 illustrate the direction change of the particle orientation observed from the top and the side views, respectively. The top view corresponds to the xz plane, while the side view is the yz plane.

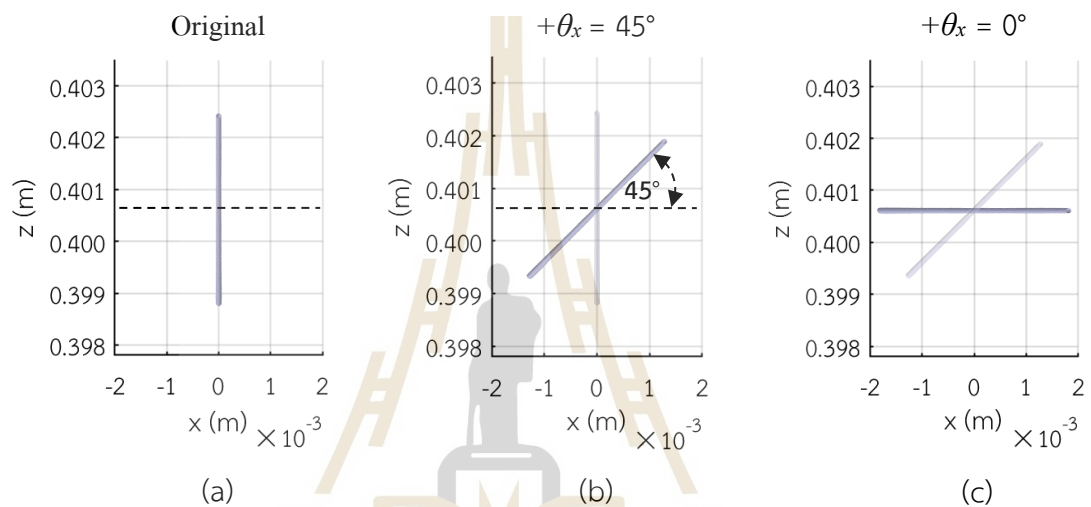


Figure 4.11 Relationship between the particle orientations and the calculated rotation angle $+\theta_x$.

Figure 4.11(a) illustrates the top view of the original particle orientation reconstructed from the digital hologram. The particle is oriented perpendicular to the x-axis or parallel to the z-axis. Figure 4.11(b) illustrates the particle orientation when there is the hand movement in the +x-axis, which produces the rotation angle $+\theta_x$ of 45°. The particle orientation is rotated by this angle with respect to the x-axis. Next, when the hand movement causes the rotation $+\theta_x = 0^\circ$ with respect to the x-axis. The particle will be oriented parallel to the x-axis as shown in Figure 4.11(c).

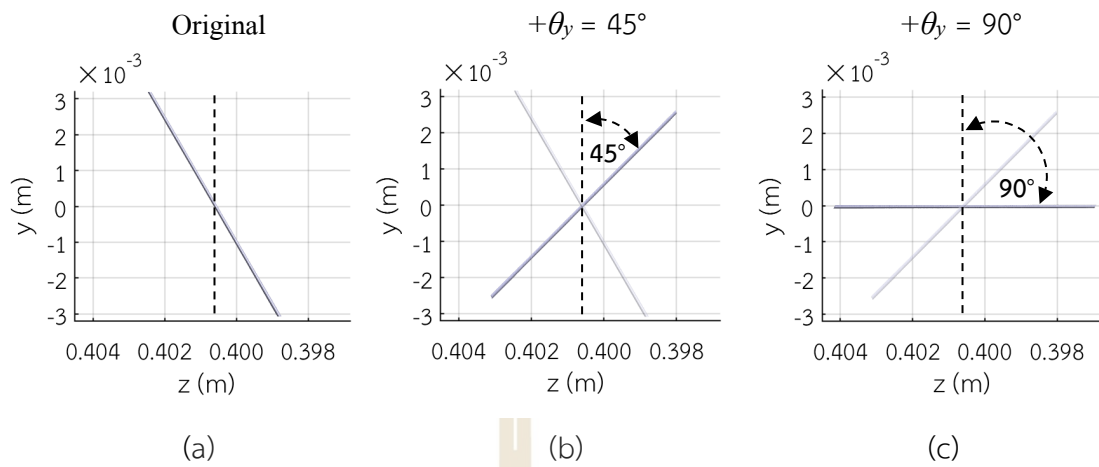


Figure 4.12 Relationship between the particle orientations and the calculated rotation angle $+\theta_y$.

Figure 4.12(a) shows the side view of the original particle orientation reconstructed from the hologram, where the middle of the particle is assumed to be located at the $y = 0$ m. Figure 4.12(a) shows the original particle orientation, which forms the angle of -30° with respect to the y -axis. In Figures 4.12 (b) and (c), the particle orientations are rotated by the angles $+\theta_y = 45^\circ$ and 90° with respect to the y -axis, respectively.

4.6 Calibrations of the webcam-based imaging setup

The webcam (OKER 386) is a manual focus camera with the sensor size of about 1/2.7 inch and the dimensions of $5.37 \times 4.04 \text{ mm}^2$. Therefore, the pixel size of the webcam can be approximately calculated as $2.797 \text{ }\mu\text{m}$. In order to obtain the best focus imaging setup, the user's hand position s_o needs to be calibrated by using a grating pattern as an input object. The grating pattern was placed away from the webcam at the position s_o varied from 20.0 cm to 80.0 cm with the interval distance Δs_o of 1 cm as shown in Figure 4.13. The best focus position s_o can be calibrated by analyzing the sharpness of the captured grating images with the LAP.

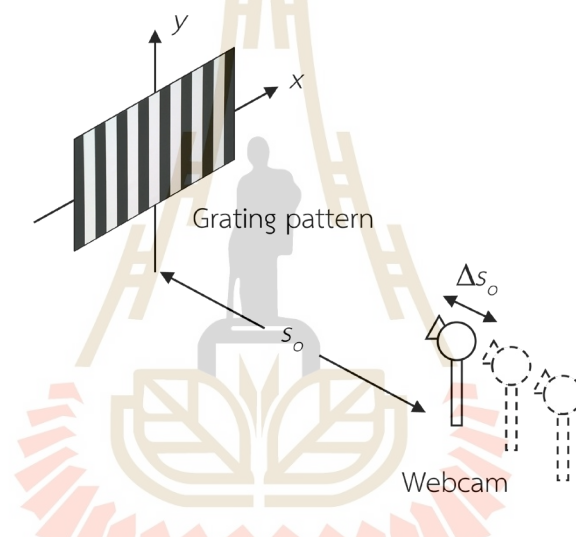


Figure 4.13 Schematic diagram of a calibration process for finding the object plane s_o in the webcam-based imaging setup.

Figure 4.13 illustrates a schematic diagram of a calibration process for finding the object plane s_o in the webcam-based imaging setup. The focus of the webcam was manually set between 2 cm – 80 cm with the focus interval of 2 cm by using Matlab function known as focus. After recording a set of grating images captured at different positions s_o , the LAP technique was used to measure the image sharpness.

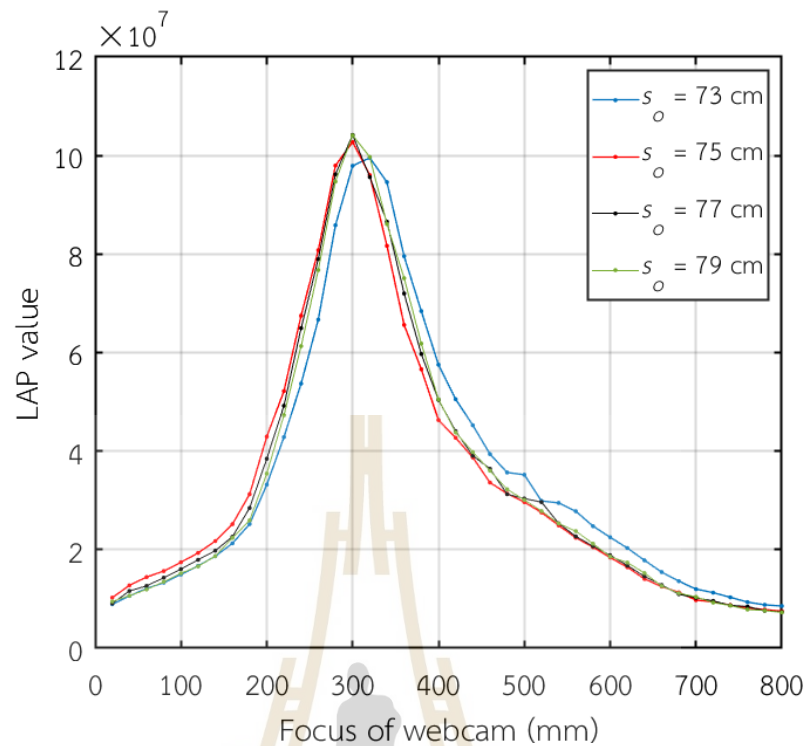


Figure 4.14 The LAP calculation from the grating pattern images at the different positions s_o as a function of the webcam focus.

Figure 4.14 shows the plots of the LAP of the grating pattern images captured at the different positions s_o , from 73 cm to 79 cm, as a function of the webcam focus. It is clear from the figure that the highest LAP peak of the captured grating appears at the position $s_o = 77$ cm with the webcam focus of 30 cm.

The next calibration is to find the array sensor position s_i or the image plane of the webcam-based imaging setup. In order to obtain the sensor position s_i , the millimeter graph paper was used as the object as shown in Figure 4.15.

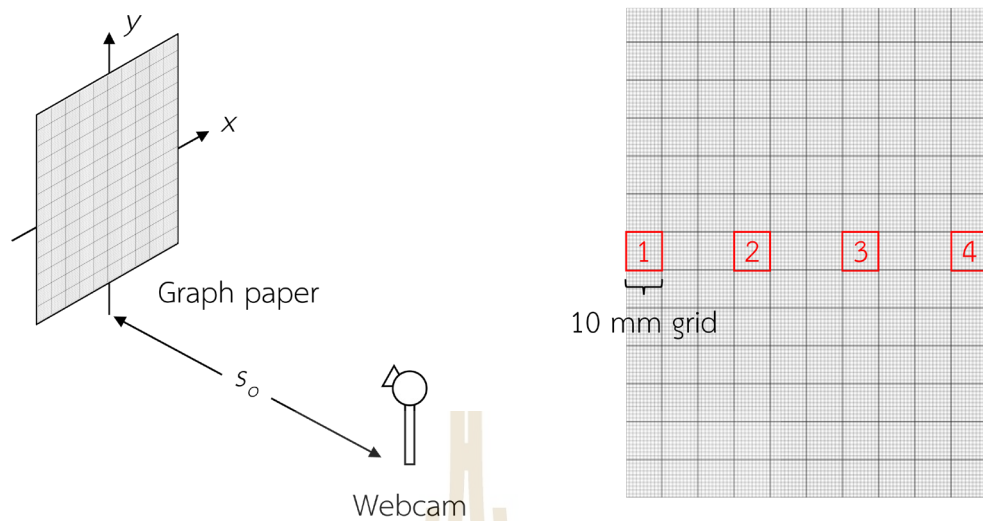


Figure 4.15 Schematic diagram of a calibration process for finding the sensor plane s_i in the webcam-based imaging setup.

The millimeter graph paper was placed at the object position $s_o = 77$ cm. Four 10-mm grids were captured as the objects by the webcam with the focus of 30 cm. The height h_i of the grid image captured by the webcam can be mathematically calculated as

$$h_i = \text{pixel size of webcam} \times np, \quad (4.1)$$

where np is the average number of the pixels contained in the image of the four grids. Since the magnification M of the imaging setup is defined as the ratio of the object size h_o to the image size h_i , the array sensor position s_i can be mathematically calculated by using the lens equation (Pedrotti *et al.*, 2012)

$$s_i = M \times s_o = \frac{h_i}{h_o} \times s_o. \quad (4.2)$$

In this case, h_o is the object height of the four 10 mm grids. The calibration result gives the sensor position s_i is equal to 0.6828 cm. Therefore, both the position s_o and the array sensor position s_i from the webcam-based imaging setup will be used in the hand

movement measurements. In summary, the hand gesture will be detected by using the proposed system at the object plane located 77 cm away from the webcam with the focus of 30 cm and the sensor position $s_i = 0.6828$ cm.

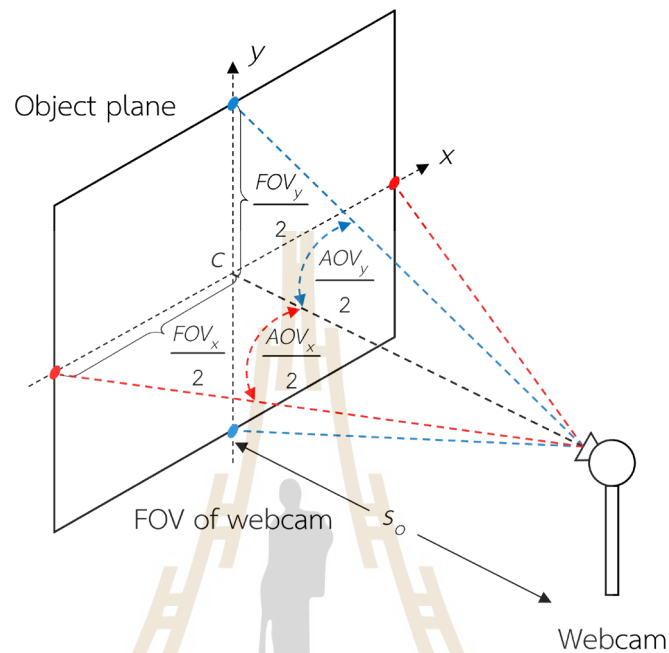


Figure 4.16 Schematic diagram of the FOV and AOV of the webcam.

In the proposed method, the translational hand movement in the object plane is captured via the external webcam of a computer. Therefore, the field of view (FOV) and angle of view (AOV) of the webcam shown in Figure 4.16 limits the measurable hand movements. In the figure, the point c corresponds to the origin of the object plane coordinate. From the lens equation, the FOVs of the webcam both along the x - and y -axes can be calculated as

$$FOV_x = \frac{\text{Number of pixels}_{x\text{-axis}} \times \text{pixel size of webcam} \times s_o}{s_i} \quad (4.3)$$

and

$$FOV_y = \frac{\text{Number of pixels}_{y\text{-axis}} \times \text{pixel size of webcam} \times s_o}{s_i} . \quad (4.4)$$

Here, FOV_x and FOV_y are the field of view along the x -axis and y -axis, respectively.

Substitutions of the object position $s_o = 77$ cm and the sensor position $s_i = 0.6828$ cm into Eqs. (4.3) and (4.4) give the values of FOV_x and FOV_y of 60.30 cm and 34.20 cm, respectively. Consequently, the two values can be used to calculate the angle of views on the x -axis and y -axis, AOV_x and AOV_y . They are found to be 42.76° and 25.04° , respectively. Therefore, the hand movement can interactively change the particle orientation angle, provided that the movements are within the field of view.

4.7 Experimental verifications of the hand detections

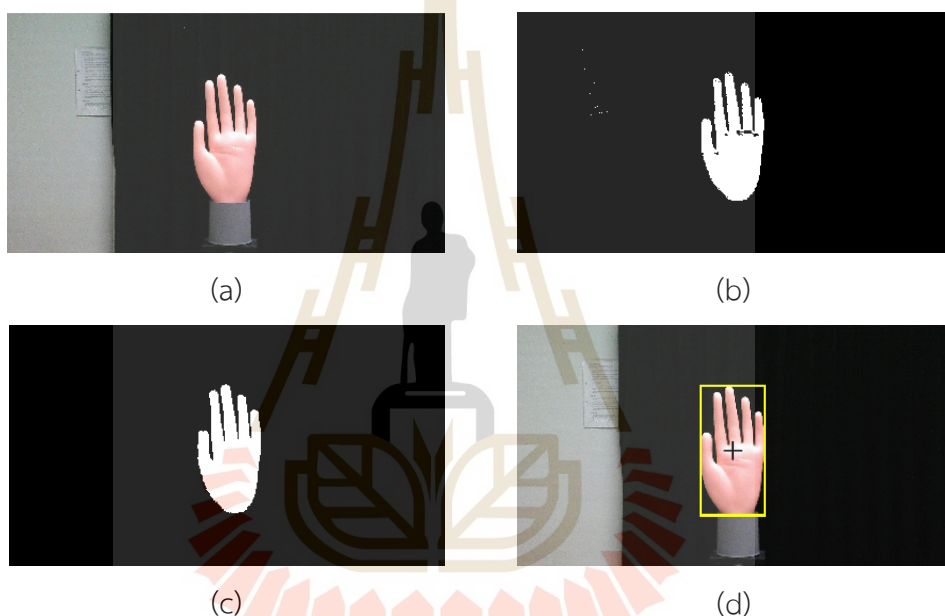


Figure 4.17 Morphological operation of the hand color image. (a) The image of the hand model from a single video frame. (b) The resultant binarized image by thresholding the HSV color space, (c) The dilated images using the disk-shaped structuring elements with a radius of 5. (d) The resultant hand detection confined by the bounding box with the hole noise removal.

In the proposed method, the morphological operation is implemented as shown in Figure 4.17. In Figure 4.17(a), the hand detection is applied to every frame of the live video captured via the webcam with the resolution is 1920×1080 pixels. After converting the RGB video frame into HSV color, the color thresholding based on HSV color adjusted the hue component to $[0.000-1.000]$, the saturation component to

[0.010 – 0.600], and the value component to [0.800 – 1.000]. The binarized image is shown in Figure 4.17(b). Figure 4.17(c) shows the result of the third step, which was the erosion operation to reduce the noise, which was followed by the dilation to improve the hand image by using the disk-shaped structuring elements with a radius of 5 pixels. The imfill function of Matlab was used to remove the noise left in the binarized image. Finally, the blob analysis extracts the hand image as a blob by using 4-connectivity as shown in Figure 4.17(d).

Table 4.4 Time measurement of the hand detections.

Webcam Resolution (pixels)	Time measurement (ms)	
	200 frames	1 frame
1920 × 1080	69,240	0.35
640 × 480	20,570	0.10

Table 4.4 presents the time measurements of the hand detection as a function of the webcam resolution. The dependency of the time measurement on the webcam resolution is caused by the fact that the morphological operation is performed in every frame on a per-pixel basis. Therefore, the higher image resolution results in a longer computational time.

4.8 Experimental measurements of the hand position

Figure 4.18 shows the experimental setup for the hand detection by using the 3-D hand model placed on an optical rail and a digital height gauge along the x- and y-axes, respectively. The hand model was used in the setup in order to have stable movements. The maximum distances of the movements along the x- and y-axes measured by using the optical rail and the digital height gauge (Moore and Wright MW190-30DBL) were –26.5 cm to +26.5 cm and –85.00 mm to +85.00 mm, respectively.

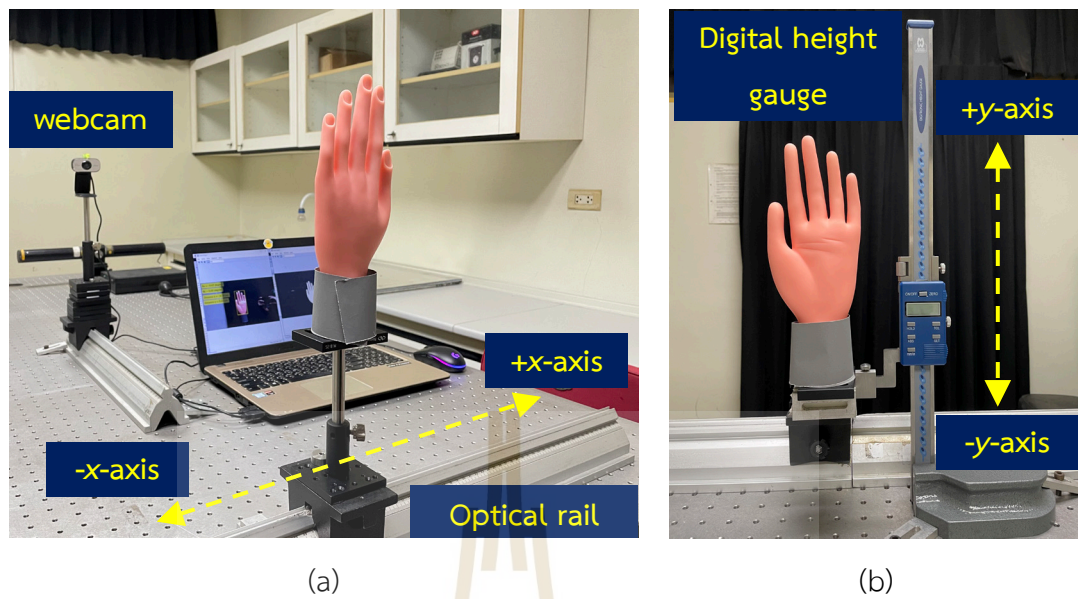


Figure 4.18 Direction of the translational hand movement along (a) the x - and (b) the y -axes detected by using the webcam.

Figure 4.19 illustrates the detected hand model confined by the bounding box. The red and the black plus symbols denote the center of the sensor plane and the bounding box, respectively.

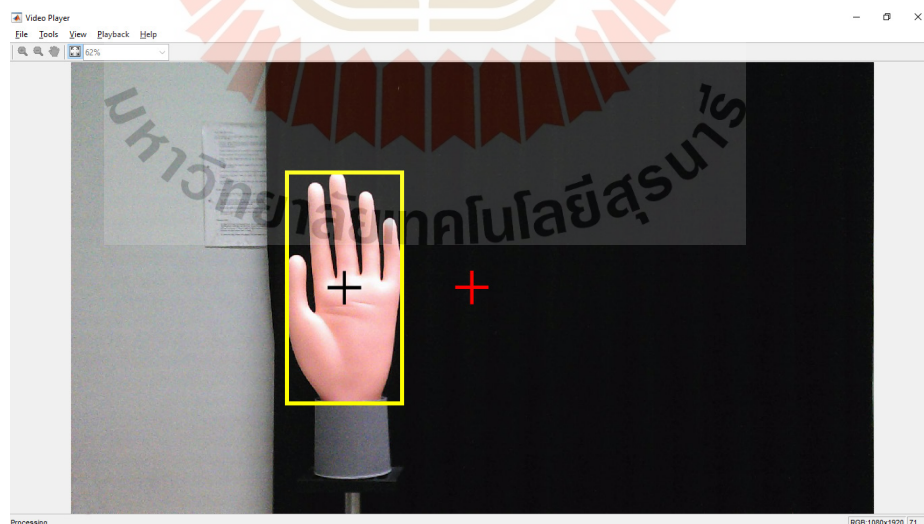


Figure 4.19 The detected hand model confined by the bounding box. The red and the black plus symbols denote the center of the sensor plane and the bounding box, respectively.

The sensitivity of the hand detection can be obtained by measuring the shortest distance movement d_y via Matlab-based hand detection. Tables 4.5 presents the results of the averaged distance measurement and its errors by using the digital height gauge. The distance measurement was varied with the interval of 1 mm. For calculating each distance d_y with Eq. (3.6), the captured 200 image frames were analyzed. The resultant calculated distances were then averaged. The results show that the movement of 10.00 mm could be detected with the mean error of 0.17%, while it is 1.3% for the 1.00 mm movement. Therefore, the longer the movement distance, the smaller the measurement errors. This may be caused by the fact that the low-cost webcam has a high f-number or a small numerical aperture. Since the size of the finest detail that can be resolved is proportional to the numerical aperture, the small aperture of the webcam cannot resolve the fine movement of the hand.

Table 4.5 Errors in the measurement of the shortest movement distance by using the digital height gauge.

Measured distance (mm)	Mean calculated distance (mm)	MAPE in the distance measurement (%)
1.00	0.987	1.3
2.00	1.98	1
3.00	2.98	0.7
4.00	3.98	0.5
5.00	4.98	0.4
6.00	5.98	0.3
7.00	6.98	0.3
8.00	7.98	0.2
9.00	8.98	0.2
10.00	9.983	0.17

Table 4.6 Errors in the measurements of the hand position $+d_x$ and its corresponding angle $+\theta_x$ by using the optical rail.

Measured Position $+d_x$ (cm)	Mean calculated $+d_x$ (cm)	Mean error (%)	Measured Angle $+\theta_x$ (°)	Mean calculated $+\theta_x$ (°)	Mean error (%)
1.0	1.008	0.8	0.7441	0.7500	0.79
2.0	1.987	0.65	1.488	1.478	0.67
3.0	2.980	0.67	2.231	2.216	0.67
4.0	3.972	0.70	2.974	2.953	0.71
5.0	4.967	0.66	3.715	3.691	0.65
6.0	5.950	0.83	4.456	4.419	0.83
7.0	6.947	0.76	5.194	5.155	0.75
8.0	7.935	0.81	5.932	5.884	0.81
9.0	8.931	0.77	6.667	6.616	0.76
10.0	9.930	0.70	7.400	7.348	0.70
11.0	10.92	0.7	8.130	8.072	0.71
12.0	11.92	0.7	8.858	8.800	0.65
13.0	12.92	0.6	9.583	9.525	0.61
14.0	13.91	0.6	10.30	10.24	0.6
15.0	14.90	0.67	11.02	10.95	0.6
16.0	15.90	0.63	11.74	11.67	0.6
17.0	16.88	0.71	12.45	12.36	0.7
18.0	17.87	0.72	13.16	13.07	0.7
19.0	18.86	0.74	13.86	13.76	0.72
20.0	19.85	0.75	14.56	14.46	0.69
21.0	20.83	0.81	15.26	15.14	0.79
22.0	21.83	0.77	15.95	15.83	0.75
23.0	22.81	0.83	16.63	16.50	0.78
24.0	23.81	0.79	17.31	17.18	0.75
25.0	24.80	0.80	17.99	17.85	0.78
26.0	25.80	0.77	18.66	18.52	0.75
26.5	26.32	0.68	18.99	18.87	0.63

Tables 4.6 and 4.7 present the detected hand positions along the +x- and +y- axes and their corresponding angles, respectively. The measured positions and angles were obtained by using the optical rail and the digital height gauge. The average values of the calculated hand positions and angles were obtained from the captured 200 video frames by using Eqs. (3.5) – (3.8). The detected hand positions in the negative axis are presented in Appendix A.

Table 4.7 Errors in the measurements of the hand position $+d_y$ and its corresponding angle $+\theta_y$ by using the digital height gauge.

Measured Position $+d_y$ (mm)	Mean calculated $+d_y$ (mm)	Mean error (%)	Measured Angle $+\theta_y$ (°)	Mean calculated $+\theta_y$ (°)	Mean error (%)
2.00	1.982	0.90	0.1488	0.1475	0.90
3.00	2.975	0.83	0.2232	0.2214	0.82
10.00	9.931	0.69	0.7441	0.7389	0.70
20.00	19.87	0.65	1.488	1.478	0.67
30.00	29.82	0.60	2.231	2.218	0.58
40.00	39.84	0.40	2.974	2.962	0.40
50.00	49.85	0.30	3.715	3.704	0.30
60.00	59.85	0.25	4.456	4.445	0.25
70.00	69.84	0.23	5.194	5.183	0.21
80.00	79.82	0.23	5.932	5.918	0.24
85.00	84.82	0.21	6.299	6.286	0.21

It is obvious that the mean errors in the measurements of the hand position and its corresponding angles by using the proposed hand detection are smaller than 1%. The main reasons for the difference between the measured and the calculated values are that, firstly, a parallax error may occur while reading the scale printed on the optical rail. The second reason is the imperfect alignment of the setup.

4.9 Experimental verifications of the Interactive imaging of 3-D microtube

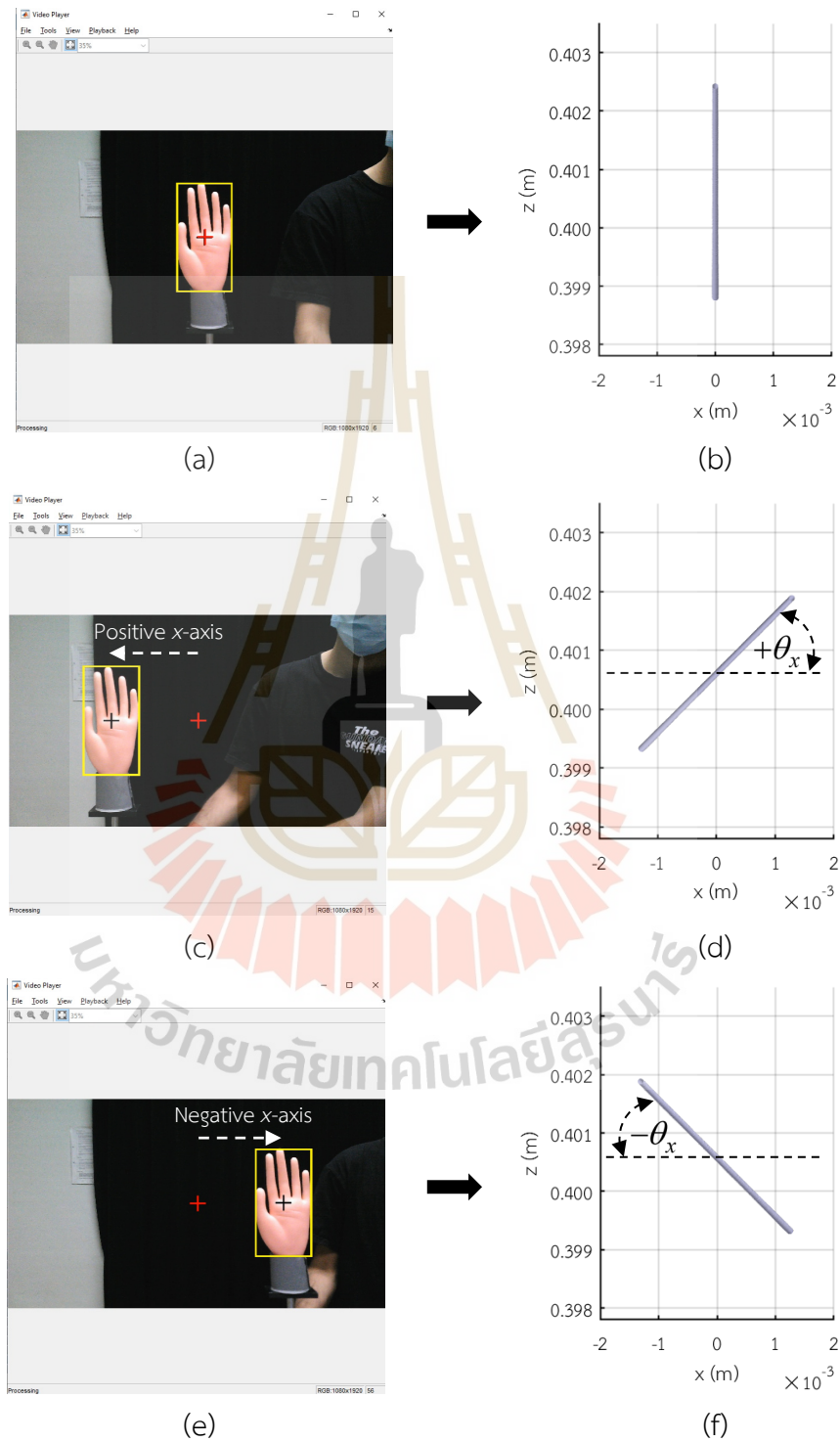


Figure 4.20 Interactive imaging of the 3-D microtube reconstructed from the digital hologram by using the hand movement along the x -axis.

Figure 4.20 shows the interactive imaging of the 3-D microtube reconstructed from the digital hologram by using hand movement along the x-axis. The microtube was recorded at the distance $z = 40$ cm with the orientation angle $= 60^\circ$. Figures 4.20(a), (c), and (e) illustrate the hand positions at the origin, the positions $+d_x$ and $-d_x$, respectively. When the hand is at the origin, the detected position $d_x = 0$ cm. The 3-D microtube image shown in Figures 4.20(b) has the same orientation as the original hologram reconstruction. When the hand moves to the position $d_x = +10.0$ cm and -10.0 cm, the bounding box center makes the angle $+\theta_x$ or $-\theta_x$ with the webcam center. They can be calculated by using Eq. (3.7), yielding the angles $\theta_x = +7.349^\circ$ and $\theta_x = -7.349^\circ$. As results, the orientations of the reconstructed 3-D microtube can be changed with respect to the x-axis as shown in Figures 4.20(d) and (f). These figures plot the top views of the 3-D microtube. In the proposed method, the last detected hand position will be used to change the particle orientation.

Figure 4.21 shows the interactive imaging of the 3-D microtube reconstructed from the same digital hologram by using the hand movement along the y-axis. Figures 4.21(a), (c), and (e) illustrate the hand positions at the origin, the positions $d_y = +8.00$ cm and -8.00 cm, respectively. In this case, Figures 4.21(b), (d), and (f) plot the corresponding side views of the 3-D microtube oriented with the angles $\theta_y = 0, +40,$ and -40 degrees, respectively, in that the rotation angles of the 3-D microtube image in the figure were interactively rotated corresponding to the last frames of the video.

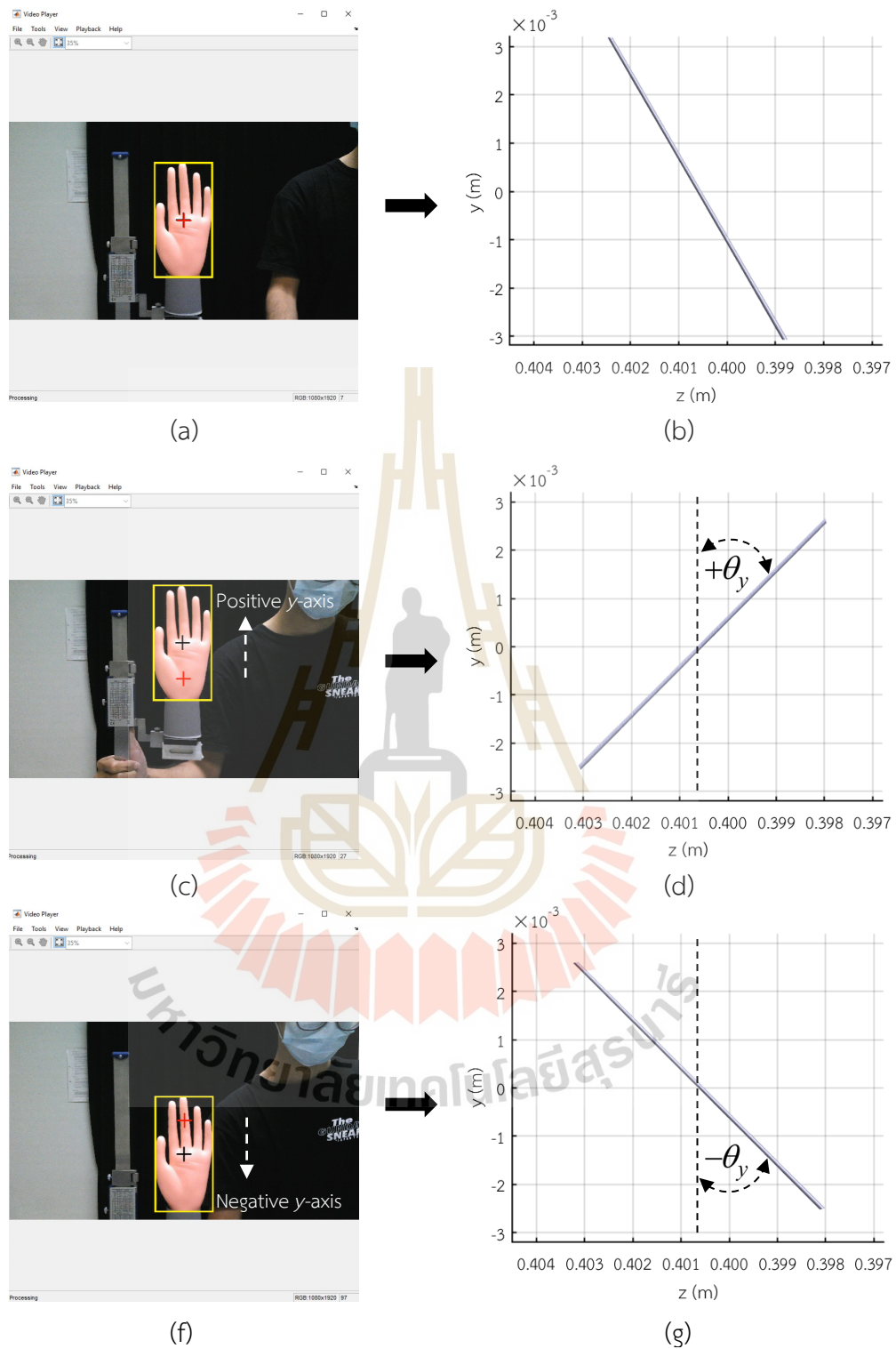


Figure 4.21 Interactive imaging of the 3-D microtube reconstructed from the digital hologram by using the hand movement along the y-axis.

CHAPTER V

CONCLUSIONS AND FUTURE WORK

5.1 Conclusions

This thesis has proposed a new method for implementing interactive 3-D visualization and morphological particle analysis reconstructed from digital holograms. The 3-D particle images are numerically reconstructed from the digital holograms, while interactive visualization is controlled by the user's hand movements detected by a low-cost webcam. The proposed method has advantages in that the interactive visualization provides not only improved visual perception but also the accuracy of morphological analysis of the particle. As a proof of concept, the interactive visualization and morphological analysis of line-shaped particle were demonstrated.

The proposed method has been experimentally verified by performing the numerical reconstructions of the 3-D particle images and the interactive visualization of the reconstructed 3-D particle images. In the first verification, the holograms of the 100 μm particle with different orientations and distances were recorded by using the array CCD image sensor. The 1-D particle images were numerically reconstructed from each row of the holograms by using the Fresnel diffraction integral. The particle depth position, size, and orientation were measured from the best in-focus reconstructed images. The experimental verifications show that the accuracy of measurements depends on the depth position, the sensor resolution, and the interval of the reconstruction distance. This is because the holograms encode the 3-D particle information as the chirp signals. The frequency of the chirp signals increases as the particle position becomes closer to the sensor. As a result, the sensor with the limited resolution cannot faithfully record the holograms. Furthermore, the LAP could find the reconstructed image with the best focus, provided that the numerical reconstructions of the holograms are done with the fine reconstruction interval.

In the second verification, the detection of the hand movements captured using the calibrated webcam was experimentally demonstrated by using the hand model. The morphological operation produced the noise-free binarized image of the hand, while the blob analysis provided the coordinate of the hand movements from each video frame captured by the webcam. Consequently, the time measurement of the interactive visualization depends on the webcam resolution. Due to the low f-number of the webcam, the shortest hand movement that could be detected with the error of less than 1% is 3 mm, corresponding to the rotation angle of 0.2214° .

5.2 Future work

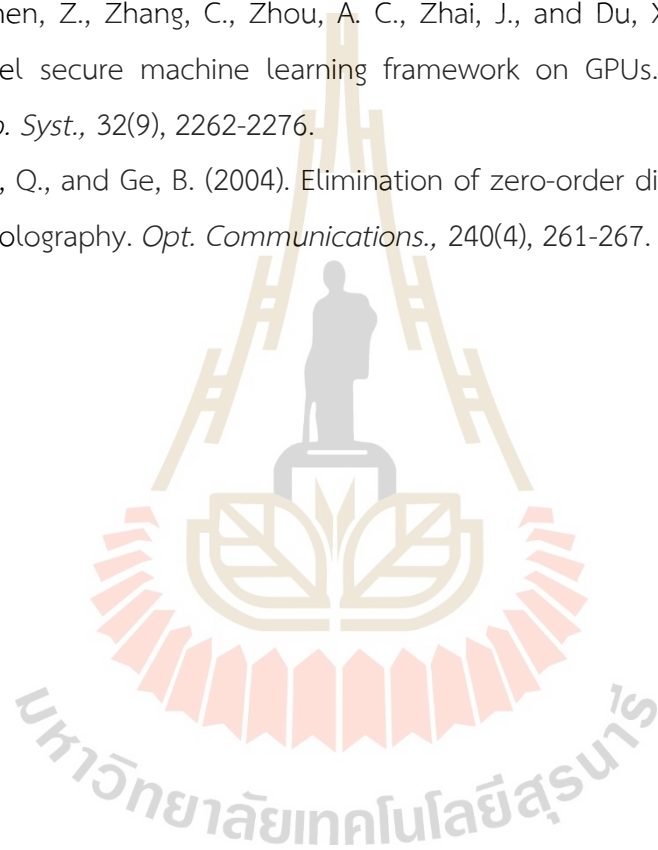
In future work, the proposed method will be applied to the analysis of non-symmetrical 3-D objects such as microorganisms. The reason for this interest is that knowledge of microbial morphology is useful for diagnosing diseases and preventing infections. To implement this application, the inline Gabor setup is modified by generating multiple inline holograms of the microorganism being studied from different illuminating angles. The multiple angles can be generated by placing the microorganism on a rotating stage or splitting light beam with beam splitters. After the microorganism profiles are numerically extracted from different illuminating angles, they are stitched to create the 3-D profile of the microorganism.

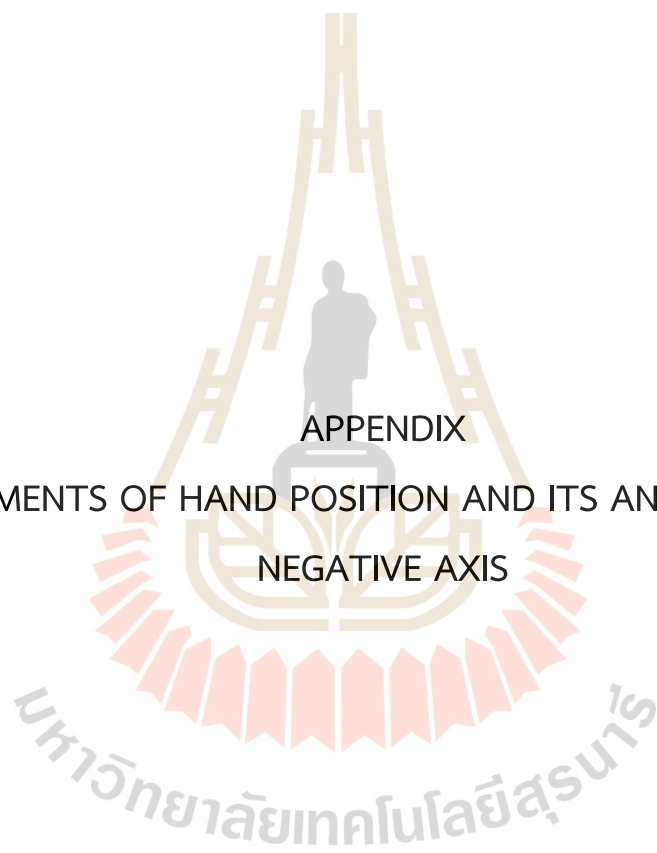
REFERENCES

- Choi, Y. K., and Lee, S. J. (2009). Three-dimensional volumetric measurement of red blood cell motion using digital holographic microscopy. *Appl. Opt.*, 48(16), 2983-2990.
- Gabor, D. (1948). A new microscopic principle. *Nature.*, 161(4098), 777-778.
- Goodman, J. W. (1996). *Introduction to Fourier optics*. McGraw-Hill.
- Hariharan, P. (1996). *Optical holography: Principles, techniques and applications*. Cambridge University Press.
- Intel Corporation. (n.d.). VR vs. AR vs. MR: What you need to know. Retrieved from <https://www.intel.com/content/www/us/en/tech-tips-and-tricks/virtual-reality-vs-augmented-reality.html>
- Javidi, B., Moon, I., Yeom, S., and Carapezza, E. (2005). Three-dimensional imaging and recognition of microorganism using single-exposure on-line (SEOL) digital holography. *Opt. Express.*, 13(12), 4492-4506.
- Kim, M. K. (2010). Principles and techniques of digital holographic microscopy. *J. Photonics Energy.*, 1(1), 018005-1-50.
- Lee, S. J., Seo, K. W., Choi, Y. S., and Sohn, M. H. (2011). Three-dimensional motion measurements of free-swimming microorganisms using digital holographic microscopy. *Meas. Sci. Technol.*, 22(6), 064004-1-8.
- Li, S., Dou, Y., Niu, X., Lv, Q., and Wang, Q. (2017). A fast and memory saved GPU acceleration algorithm of convolutional neural networks for target detection. *Neurocomputing.*, 230, 48-59.
- Memmolò, P., Miccio, L., Merola, F., Gennari, O., Netti, P. A., and Ferraro, P. (2014). 3D morphometry of red blood cells by digital holography. *Cytometry A.*, 85(12), 1030-1036.

- Merola, F., Miccio, L., Memmolo, P., Caprio, G. D., Galli, A., Puglisi, R., Balduzzi, D., Coppola, G., Netti, P., and Ferraro, P. (2013). Digital holography as a method for 3D imaging and estimating biovolume of motile cells. *Lab Chip.*, 13(23), 4512-4516.
- Microsoft Corporation. (2022). *What is mixed reality?* Retrieved from <https://docs.microsoft.com/en-us/windows/mixed-reality/discover/mixed-reality>
- Moeslund, T. B. (2012). *Introduction to video and image processing building real systems and applications*. Springer.
- Naqwi, A., Durst, F., and Kraft, G. (1991). Sizing of submicrometer particles using a phase Doppler system. *Appl. Opt.*, 30(33), 4903–4913.
- Pedrotti, F. L., Pedrotti, L. M., and Pedrotti, L. S. (2006). *Introduction to optics*. Addison-Wesley.
- Rock, I., Halper, F., and Clayton, T. (1972). The perception and recognition of complex figures. *Cogn. Psychol.*, 3(4), 655-673.
- Stratmann, L. (2022). *Conceptualization and prototypical implementation in WebGL of an exercise in color theory*. Retrieved from <http://color.lukas-stratmann.com>
- The MathWorks. (2022). *Morphological structuring element - MATLAB*. Retrieved from <https://www.mathworks.com/help/images/ref/strel.html>
- Tian, L., Loomis, N., Dominguez-Caballero, J. A., and Barbastathis, G. (2010). Quantitative measurement of size and three-dimensional position of fast-moving bubbles in air–water mixture flows using digital holography. *Appl. Opt.*, 49(9), 1549-1554.
- Tyler, G. A., and Thompson, B. J. (1976). Fraunhofer holography applied to particle size analysis a reassessment. *Opt. Acta.*, 23(9), 685-700.
- Viola, P., and Jones, M. (2001). Rapid object detection using a boosted cascade of simple features. *Proc. IEEE Comput. Soc. Conf. Comput. Vis. Pattern Recognit.*, 1, 511-518.
- Yamashita, R., Nishio, M., Do, R. K., and Togashi, K. (2018). Convolutional neural networks: An overview and application in radiology. *Insights Imaging.*, 9(4), 611-629.

- Yamazaki, A., Ito, T., Sugimoto, M., Yoshida, S., Honda, K., Kawashima, Y., Fujikawa, T., Fujii, Y., Tsutsumi, T. (2021). Patient-specific virtual and mixed reality for immersive, experiential anatomy education and for surgical planning in temporal bone surgery. *Auris Nasus Larynx.*, 48(6), 1081-1091.
- Yu, X., Hong, J., Liu, C., Cross, M., Haynie, D. T., and Kim, M. K. (2014). Four-dimensional motility tracking of biological cells by digital holographic microscopy. *J. Biomed. Opt.*, 19(4), 045001-1-9.
- Zhang, F., Chen, Z., Zhang, C., Zhou, A. C., Zhai, J., and Du, X. (2021). An efficient parallel secure machine learning framework on GPUs. *IEEE Trans. Parallel Distrib. Syst.*, 32(9), 2262-2276.
- Zhang, Y., Lü, Q., and Ge, B. (2004). Elimination of zero-order diffraction in digital off-axis holography. *Opt. Communications.*, 240(4), 261-267.





APPENDIX

MEASUREMENTS OF HAND POSITION AND ITS ANGLE ALONG THE
NEGATIVE AXIS

APPENDIX A

Table A.1 Errors in the measurements of the hand position $-d_x$ and its corresponding angle $-\theta_x$ by using the optical rail.

Measured Position $-d_x$ (cm)	Mean calculated $-d_x$ (cm)	Mean error (%)	Measured Angle $-\theta_x$ (°)	Mean calculated $-\theta_x$ (°)	Mean error (%)
1.0	0.9940	0.60	0.7441	0.7396	0.6
2.0	1.988	0.60	1.488	1.479	0.6
3.0	2.978	0.73	2.231	2.215	0.72
4.0	3.967	0.83	2.974	2.949	0.84
5.0	4.961	0.78	3.715	3.686	0.78
6.0	5.955	0.75	4.456	4.422	0.76
7.0	6.947	0.76	5.194	5.155	0.74
8.0	7.940	0.75	5.932	5.887	0.76
9.0	8.943	0.63	6.667	6.625	0.63
10.0	9.931	0.69	7.400	7.349	0.69
11.0	10.92	0.7	8.130	8.072	0.72
12.0	11.91	0.7	8.858	8.793	0.73
13.0	12.92	0.6	9.583	9.525	0.60
14.0	13.91	0.6	10.30	10.24	0.6
15.0	14.92	0.5	11.02	10.97	0.5
16.0	15.90	0.63	11.74	11.67	0.6
17.0	16.89	0.65	12.45	12.37	0.6
18.0	17.88	0.67	13.16	13.07	0.7
19.0	18.90	0.53	13.86	13.79	0.5
20.0	19.90	0.50	14.56	14.49	0.5
21.0	20.87	0.62	15.26	15.17	0.6
22.0	21.85	0.68	15.95	15.84	0.68
23.0	22.84	0.70	16.63	16.52	0.66
24.0	23.83	0.71	17.31	17.20	0.66
25.0	24.83	0.68	17.99	17.87	0.67
26.0	25.81	0.73	18.66	18.53	0.70
26.5	26.31	0.72	18.99	18.86	0.66

Table A.2 Errors in the measurements of the hand position $-d_y$ and its corresponding angle $-\theta_y$ by using the digital height gauge.

Measured Position $-d_y$ (mm)	Mean calculated $-d_y$ (mm)	Mean error (%)	Measured Angle $-\theta_y$ (°)	Mean calculated $-\theta_y$ (°)	Mean error (%)
10.00	9.930	0.70	0.7441	0.7389	0.70
20.00	19.90	0.50	1.488	1.480	0.5
30.00	29.87	0.43	2.231	2.222	0.4
40.00	39.84	0.40	2.974	2.962	0.40
50.00	49.87	0.26	3.715	3.706	0.2
60.00	59.85	0.25	4.456	4.445	0.25
70.00	69.85	0.21	5.194	5.183	0.21
80.00	79.82	0.23	5.932	5.918	0.24
85.00	84.78	0.26	6.299	6.283	0.25

Table A.1 and Table A.2 present the detected hand position and its corresponding angles along the negative x - and y -axes. The average values of the calculated positions ($-d_x$ and $-d_y$) and their angles ($-\theta_x$ and $-\theta_y$) were obtained from 200 video frames of the hand movements by using the blob analysis and Eqs. (3.5) – (3.8). The mean errors in both the calculated position and its angles reveal that they are less than 1%. They are caused by similar reasons as explained in Tables 4.6 and 4.7. The mean errors of the movement along the y -axis are better than the movement along the x -axis. This is because the digital height gauge scale has a higher resolution and provides easy and stable movement of the hand model.

CURRICULUM VITAE

Name : Mr. Sangchai Paijit

Date of Birth : April 28, 1996

Place of Birth : Sing Buri, Thailand

Address : 190/102, Village No. 1, Bang Krabue sub-district, Mueang Sing Buri district,
Sing Buri province, 16000, Thailand.

Email : sangchai.g@gmail.com

Education background : Bachelor of Engineering Program in Electronic Engineering,
Suranaree University of Technology.

Publications :

- Paijit, S., and Widjaja, J. (2022). 3-D Morphological Analysis of Line-Shaped Particle from Digital In-line Holograms. *In Proceedings of the 2022 International Electrical Engineering Congress*, 1-4. doi: 10.1109/IEECON53204.2022.9741693

Grants and Fellowships :

- External Grants and Scholarships for Graduate Students from Institute of Research and Development, Suranaree University of Technology.

มหาวิทยาลัยเทคโนโลยีสุรนารี